On the Relative Stability of Near-Surface Oxygen Vacancies at the CeO_2(111) Surface upon Zr Doping

G. S. Otero[†], P. Lustemberg[‡,§*], F. Prado[†], and M. V. Ganduglia-Pirovano[§]

[†]Departamento de Física, Universidad Nacional del Sur and IFISUR, CONICET, Av. L.N. Alem 1253, B8000CPB, Bahía Blanca, Buenos Aires, Argentina

[‡]Instituto de Física Rosario (IFIR-CONICET) and Universidad Nacional de Rosario (UNR), Ocampo y Esmeralda, S2000EKF Rosario, Santa Fe, Argentina

[§]Instituto de Catálisis y Petroleoquímica (ICP-CSIC), C/Marie Curie 2, 28049 Madrid, Spain

ABSTRACT

The effects of Zr doping on the stability of the CeO_2(111) surface as a function of the dopant concentration and distribution, as well as on the relative stability of surface and subsurface oxygen vacancies, were studied by means of density functional theory (DFT+U) calculations. For a given Zr content, the more stable structures do not correspond to those configurations with Zr located in the topmost O-Ce-O trilayer (TL1), but in inner layers, and the stability decreases with increasing Zr concentration. For the undoped CeO_2(111) surface, the preference of subsurface vacancies with next-nearest neighbor (NNN) Ce^{3+} configuration has earlier been predicted. For the Zr-doped surface, the formation of vacancies was studied using a surface unit cell with 2×2 periodicity, and it was found that the most stable configuration corresponds to the Zr atom located in the surface layer (TL1) neighboring a subsurface oxygen vacancy with NNN Ce^{3+}, being the formation energy equal to 1.16 eV. The corresponding surface oxygen vacancy is 0.16 eV less stable. These values are by 0.73 and 0.92 eV, respectively, smaller than the corresponding ones for the pure CeO_2(111) surface. Moreover, when Zr is located in TL2 the subsurface vacancy becomes by 0.10 eV less stable, compared to Zr in the TL1. The Ce^{3+} preference for the next-nearest neighbor cationic sites to both surface and subsurface vacancies at CeO_2 (111), becomes more pronounced upon Zr doping. The results are explained in terms of Zr- and vacancy-induced lattice relaxation effects.

This is the version submitted to jpc c on october 7, 2019

1. INTRODUCTION

Ceria (CeO_2)-based materials are of great importance in numerous technological applications such as three-way catalysts (TWCs) [1,2], hydrocarbon reforming [2,3] and solid oxide fuel cells (SOFC) [2,3]. These materials possess a property that is key to most of such applications, namely, their capability for easy conversion between the Ce^{4+} and Ce^{3+} oxidation states, which is achieved by releasing oxygen atoms from the crystal lattice and forming oxygen vacancies. Thus, the energy needed to create such oxygen vacancies is of high relevance to the description of the catalytic behavior of ceria-based materials during chemical reactions on their surfaces. Moreover, the solid solution of CeO_2 with other oxides has been extensively explored in order to develop more efficient catalysts [4-6]. In particular, the replacement of Ce by Zr to form CeO_2-ZrO_2 solid solutions was found to facilitate the reducibility of the oxide [7-9] as well as to increase the oxygen storage capacity and the system thermal stability, compared to pure CeO_2, leading to the use of $Ce_{1-x}Zr_xO_2$ materials as TWCs. More recently, $Ce_{1-x}Zr_xO_2$ samples were explored as catalysts for CO and HCl oxidation [10], the direct oxidation of methane [11-13], and for solar thermochemical water splitting [14]. For the CO and HCl oxidation, the maximum activity was found for $Ce_{1-x}Zr_xO_2$ with x=0.2 [10]. The highest values of methane conversion were reported for x = 0.1 [13], whereas for thermochemical water splitting [14], the optimal composition was found to be in the Zr range of $0.15 \leq x \leq 0.2$, which also avoids the crystal structure transformation from the cubic fluorite to the tetragonal phase [15]. In all cases, the higher reducibility of $Ce_{1-x}Zr_xO_2$ compared to CeO_2 was indicated as responsible for the enhanced performance of the doped ceria system.

Theoretical works have correlated the improved reducibility of Zr-doped ceria systems with the decrease in the oxygen vacancy formation energy (E_f) near Zr cations [16-26]. For instance, Yang et al. [16,17], using DFT+U [27] (U is an effective onsite Coulomb correction), reported a decrease of 0.65 and 0.52 eV in the formation energy of vacancies created next to Zr cations in $Ce_{0.97}Zr_{0.03}O_2$ and at the Zr-doped CeO_2(111) surface, respectively. A similar result was reported by Hu and Metiu [18] who also investigated the Zr-doped CeO_2(111) surface and obtained a corresponding reduction of 0.8 eV (DFT+U) when a surface oxygen vacancy is created near the dopant. Moreover, they also concluded that the influence of Zr has a very local character, i.e., Zr does not affect the energy of vacancy formation in the surface layer if it is located in inner layers far from the vacancy. Furthermore, calculations as a function of the Zr content in $Ce_{1-x}Z_xO_2$ solid solutions have revealed the fundamental role of structural relaxations, which follow the doping by Zr and the subsequent creation of a vacancy, in determining its formation energy [19,21,22], and reported the minimum value of E_f for x = 0.5 [19]. Lattice relaxations have also

This is the version submitted to jpc c on october 7, 2019

been invoked to explain the lower chemical expansion of $Ce_{0.5}Zr_{0.5}O_2$ compared to CeO_2 [28], and in addressing the formation of oxygen vacancies at the Zr-doped CeO_2(111) surface [17,18]. Finally, Weck et al. [29], using DFT+U, have considered selected $Ce_{1-x}Zr_xO_2$ surfaces and the $Ce_{1-x}Zr_xO_2/CeO_2$ interface and found that both the surface and interface fracture energies increase with the Zr content as well as highlighted the importance of surface relaxation upon interface cracking.

Another matter of interest is related to the localization of the excess electrons left in ceria-based materials upon oxygen removal, driving the $Ce^{4+} \rightarrow Ce^{3+}$ reduction. It was initially proposed that in pure CeO_2, the excess electrons localize at nearest neighbor Ce ions to the vacancies [30,31]. However, later studies have indicated that for undoped CeO_2 bulk [21,32-35] and its (111) surface [36-39], the preference of the excess charge is to localize at next-nearest neighbor cationic sites to the vacancies. In addition, for the (111) surface, the higher stability of subsurface oxygen vacancies, as compared to surface ones, has been established [38,40-42]. As yet, studies on reduced Zr-doped ceria systems that mention the location of the Ce^{3+} ions are relatively scarce [16,17,21,22] and all of them –with the exception of one considering reduced κ-$Ce_2Zr_2O_8$ [21] –reported structures in which the Ce^{3+} are nearest-neighbor to the vacancies, and there has been no systematic study considering different configurations for the excess charge. Furthermore, to the best of our knowledge, there is no study addressing the relative stability of surface and subsurface oxygen vacancies at the Zr-doped CeO_2(111) surface. Which is the most stable configuration of the excess-charge for the reduced Zr-doped CeO_2(111) surface? Also, are subsurface oxygen vacancies still more stable than surface ones upon doping? Considering the surface chemistry of Zr-doped ceria, the answers to these questions cannot be ignored.

Herein, we investigate the effects of Zr doping on the stoichiometric and reduced CeO_2(111) surface using DFT+U calculations to determine the preferred location of Zr dopants at various concentrations and to pinpoint how Zr doping affects the stability of near-surface oxygen vacancies –including the position of the Ce^{3+} ions. The results are analyzed considering the lattice relaxations induced by the presence of dopants as well as by the creation of vacancies, and are compared to those for the undoped CeO_2(111) surface.

2. METHODS AND MODELS

Spin-polarized DFT calculations were carried out using the slab–supercell approach [43], with the Vienna Ab-initio Simulation Program (VASP, http://www.vasp.at; version vasp.5.3.5) [44,45]. We explicitly treated the Ce (4f, 5s, 5p, 5d, 6s), O (2s, 2p) and Zr (4d, 5s) electrons as valence states within the projector augmented wave (PAW) method with a plane-wave cutoff energy of

415 eV, whereas the remaining electrons were considered as part of the atomic core. Strong correlation effects due to charge localization were modeled by adding a Hubbard U-like term [27] (U_{eff}= U-J, i.e., the difference between the Coulomb U and exchange J parameters, from now on referred to simply as U) to the Perdew, Burke and Ernzerhof (PBE) generalized gradient approximation (GGA) functional [46]. We used a value of U = 4.5 eV for the Ce 4f states [47,48].

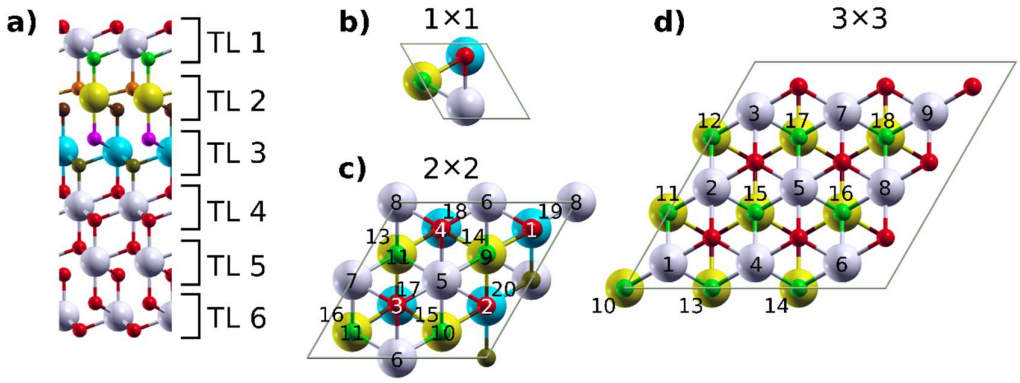

Figure 1. Supercells of the (111)-oriented slabs used in the calculations. The colors differentiate the atomic layers: red, green, orange, brown, pink and olive are oxygen atoms, whereas white, yellow, and cyan are Ce atoms. a) Side view of a slab indicating the different trilayers. Top view of the b) 1×1 cell, c) 2×2 surface unit cell with labeled atoms used as reference for the locations of oxygen vacancies, Zr dopant and Ce^{3+} ions. d) Top view of the 3×3 cell. This atom color code is used hereinafter.

The CeO_2(111) surface was modeled employing unit cells with 1×1, 2×2 and 3×3 periodicities (see Fig. 1) and (6×6×1), (3×3×1) and (2×2×1) k-point meshes, respectively, selected using the Monkhorst−Pack method [49].The 1×1, 2×2 and 3×3 supercells contained 6, 5, and 4 O-Ce-O trilayers (TL), respectively, with calculated cubic CeO_2 bulk lattice constant (a=5.485 Å) and a vacuum layer of at least 10 Å. The surface unit cell and the bottom trilayer were kept fixed during geometry optimization, whereas the rest of the atoms were allowed to fully relax.

The Zr-doped CeO_2(111) surface energy was studied for a wide range of dopant concentrations, measured as the ratio between the actual number of Zr atoms in the supercell and the number of Zr atoms needed to fully dope one cationic layer within that cell, completing the monolayer (1 ML). Thus, in the cases of the 1×1 cell with one Zr atom in different trilayers, the Zr concentration is always 1 ML, whereas for the 2×2 with up to four Zr, and 3×3 cells with one, two, and nine Zr, the concentrations are 0.25, 0.5, 0.75 and 1 ML, and 0.11, 0.22and 1 ML, respectively.

To determine the relative stability of Zr-doped CeO_2(111) surfaces, we calculated the change in the surface energy upon doping as:

$$\Delta\Gamma = \frac{1}{A}\left[E_{Zr_mCe_nO_{2(n+m)}} - E_{Ce_{n+m}O_{2(n+m)}} - mE_{ZrO_2}^{bulk} + mE_{CeO_2}^{bulk}\right] \quad (1),$$

where *A* is the area of the surface unit cell, $E_{Zr_mCe_nO_{2(n+m)}}$ is the energy of the Zr-doped CeO_2(111) slab, $E_{Ce_{n+m}O_{2(n+m)}}$ is the energy of the corresponding undoped system, and m,n indicate the number of Ce and Zr atoms in the slabs, respectively. $E_{CeO_2}^{bulk}$ and $E_{ZrO_2}^{bulk}$ are the energies per formula unit of the cubic (fluorite) CeO_2 and ZrO_2 bulk (a=5.17Å) cells (M_4O_8 composition), respectively.

The 2×2 unit cell, but with 4 TL, was used to model the presence of surface and subsurface oxygen vacancies within the outermost O-Ce-O trilayer (TL1) of the stoichiometric and Zr-doped CeO_2(111) surfaces. In order to inspect different configurations of the reduced Ce^{3+} sites, a two-step relaxation procedure was applied. In the first step, we replaced two selected Ce^{4+} by La^{3+} ions (with a larger ionic radii) per O vacancy and performed non-spin-polarized calculations. The so-obtained relaxed structure was further optimized using the regular Ce^{4+} PAW potentials. We limit the discussion to high-spin states because the difference between these states and any other spin state is less than 0.01 eV.

The oxygen vacancy formation energy (E_f) was calculated as:

$$E_f = E_{Zr_mCe_nO_{2(n+m)-1}} + \frac{1}{2}E_{O_2} - E_{Zr_mCe_nO_{2(n+m)}} = E_f^{unrelax} - E_f^{relax} \qquad (2),$$

where $E_{Zr_mCe_nO_{2(n+m)-1}}$ is the total energy of the reduced slab with an oxygen vacancy, E_{O_2} is the energy of the gas phase O_2 molecule, and $E_{Zr_mCe_nO_{2(n+m)}}$ is the energy of the unreduced slab. E_f can also be written as the difference of two terms $E_f = E_f^{unrelax} - E_f^{relax}$, in which $E_f^{unrelax}$ is the energy required to remove an oxygen atom with fix structure, and E_f^{relax} (> 0) is the energy gained from structural relaxation in the presence of the oxygen vacancy.

3. RESULTS AND DISCUSSION

3.1 Effect of Zr on the Surface Stability

The stability of the (Ce,Zr)O_2(111) surfaces was studied using equation (1) and employing the 1×1, 2×2 and 3×3 supercells displayed in Figure 1. In the calculations with the 1×1 surface unit cell, the Ce cation was replaced by a Zr atom in TL1 and subsequent trilayers till TL4, obtaining in each case a complete monolayer (ML) of Zr. Figure 2 shows the variation of the calculated changes in the surface energy for the cases in which the atoms were kept fixed according to their coordinates in the undoped CeO_2(111) surface (unrelaxed data), as well as after geometry optimization (relaxed data). The highest surface energy change for the unrelaxed slabs, $\Delta\Gamma_{unrelax}$= 1.552 J/m^2, was obtained for the Zr atom located in the outermost trilayer (TL1). As the Zr

This is the version submitted to jpc c on october 7, 2019

location moves towards the bulk, $\Delta\Gamma_{unrelax}$ decreases to ~1.0 J/m^2. When the surface is allowed to relax, the same trend is observed (Figure 2); $\Delta\Gamma$ is reduced by 0.549 J/m^2 for Zr in TL1, whereas for Zr in TL2-TL4 the reduction is somewhat larger, i.e. about 0.65-0.70 J/m^2. The higher surface energy change obtained for Zr located at the surface (TL1), as compared to the cases in which Zr is located in deeper trilayers (TL2-TL4), correlates to the fact that the Zr^{4+} dopant in the cubic (fluorite) structure, prefers to bind to 8 oxygen ions instead of 7, as it is the case in the TL1. The lowest value, $\Delta\Gamma_{relax}$ = 0.330 J/m^2, was obtained for the Zr located in TL2, although the difference with the values for Zr located in deeper trilayers is small. Thus, upon Zr doping, the concentration of Zr in the surface layer is expected to be lower than in deeper layers, with a certain preference for the near-surface region.

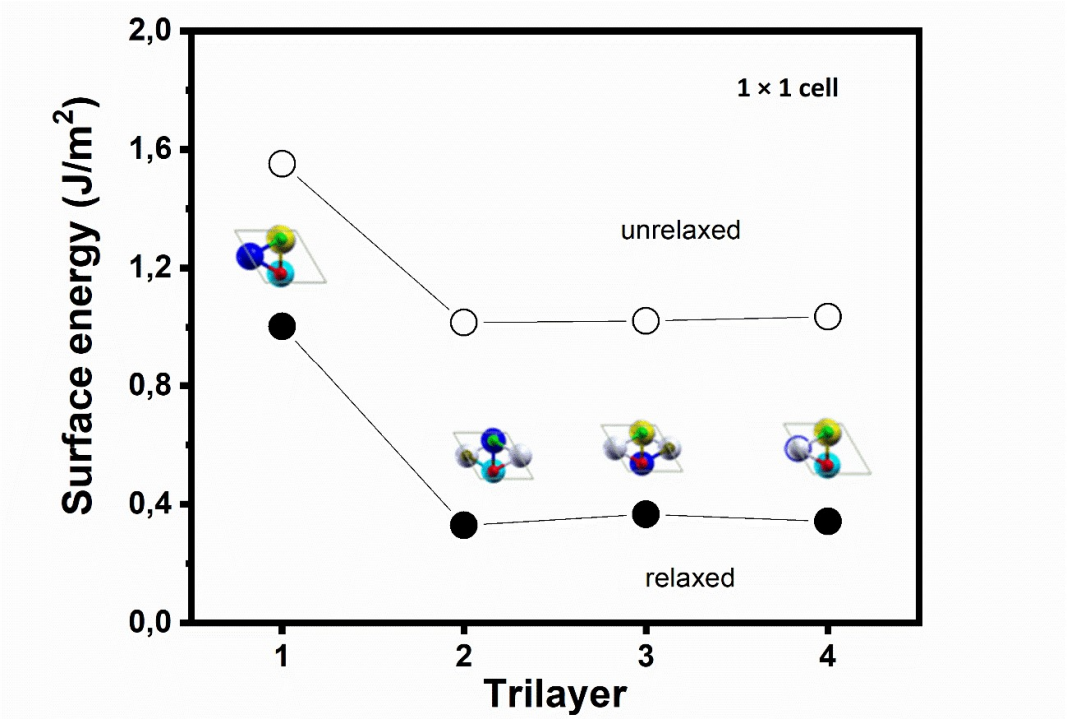

Figure 2: Change in the surface energy upon Zr doping (eq 1) using a 1×1 supercell. The location of the Zr atom varies from the surface (TL1) towards deeper layers. Open and closed symbols correspond to the unrelaxed and relaxed surfaces, respectively. The top views of the doped slabs showing the Zr position (in blue) are also included (cf. Figs. 1a and b).

The influence of the location of Zr dopants, either in the surface layer or in deeper layers, on the change in the surface energy was also analyzed for the lower Zr concentrations of 0.11, 0.22, 0.25, 0.5, and 0.75 ML (Figure 3 and Table S1), using units cells with a 3×3 and a 2×2 periodicities. Moreover, selected configurations with not all of the Zr dopants in the same trilayer were also evaluated. Furthermore, using the 2×2 unit cell, selected configurations with four Zr dopants (1

ML) distributed in the outermost three trilayers were also considered. In nearly all cases, the lowest $\Delta\Gamma$ value for the relaxed (unrelaxed) structures corresponds to configurations where the Zr atoms are located in TL2 (Figure 3 and Table S1), with $\Delta\Gamma_{relax}$ = 0.053, 0.105, 0.118, 0.218 and 0.289 J/m^2 ($\Delta\Gamma_{unrelax}$ = 0.119, 0.237, 0.247, 0.473 and 0.696 J/m^2) for 0.11, 0.22, 0.25, 0.5 and 0.75 ML, respectively. The surface energy is smallest for the lowest Zr concentration and largest for the highest concentration, i.e., the correlation between $\Delta\Gamma$ and Zr concentration is positive for both the relaxed and unrelaxed structures (Figure 3). Moreover, the amount by which the surface energy decreases due to lattice relaxations following Zr-doping, increases with increasing Zr concentration. For instance, for the structures with all dopants in TL2 and 2×2 periodicity, the surface energy is lowered by 0.129, 0.255, and 0.407 J/m^2 for a Zr concentration of 0.25, 0.5, and 0.75 ML, respectively (Figure 3 and Table S1).

Furthermore we note that the calculated $\Delta\Gamma$ values for 1 ML and different distributions of the dopants with 2×2 periodicity (Table S1), appears to suggest that a more homogeneous distribution of the dopants between the TL2 and TL3 might be to a small degree energetically preferred than having a full Zr layer near the surface in TL2, which would be strained. The reason for the preference is likely due to the better ability of the system to release lattice strain in the preferred configurations. (We recall that the surface unit cell is fixed during geometry optimization.) In addition, for the Zr concentration of 0.22 ML with 3×3 periodicity (Table S1), two arrangements of Zr atoms in TL1 as well as in TL2 were analyzed. The first arrangement corresponds to two nearest neighbor Zr atoms at a distance of ~384 pm in the cationic plane, such as Zr^1 and Zr^2 (Figure 1d), and the second one to two next-nearest neighbor Zr atoms at a distance of ~ 672 pm, such as Zr^1 and Zr^5 (Figure 1d). For the closest and next-nearest neighbor Zr pairs in TL1, the calculated $\Delta\Gamma$ values are $\Delta\Gamma_{relax}$ = 0.166 and 0.155 J/m^2, respectively, whereas for the corresponding pairs in TL2 the values are $\Delta\Gamma_{relax}$= 0.105 and 0.102 J/m^2. These values suggest no preference for Zr clustering at the CeO_2(111) surface.

This is the version submitted to jpc c on october 7, 2019

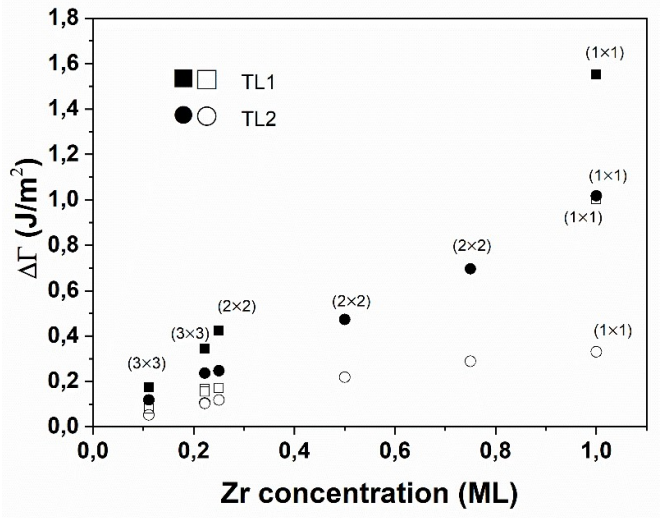

Figure 3: Calculated change in the surface energy, $\Delta\Gamma$, as a function of Zr concentration. The cell used for each data point (1×1, 2×2 or 3×3) is indicated. Filled (open) symbols correspond to the unrelaxed (relaxed) surfaces with Zr dopants in the same trilayer (cf. Table S1 for the precise location of the Zr atoms in the structures according to Figure 1, and the $\Delta\Gamma$ values for all structures considered).

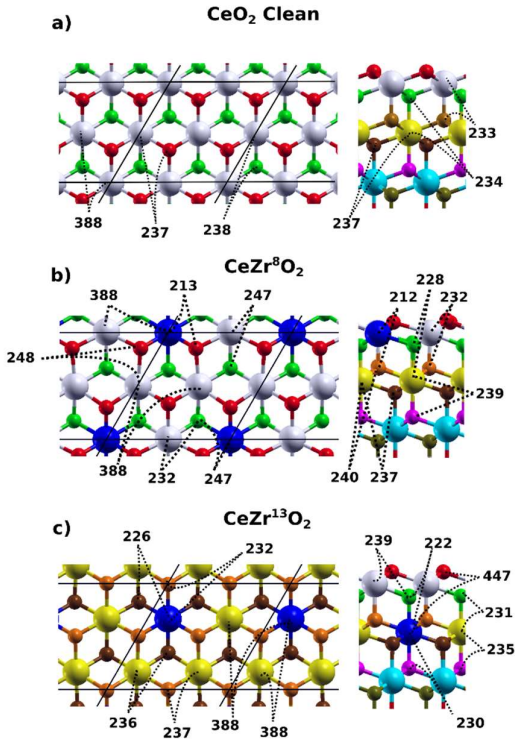

Figure 4: Top and side views of the relaxed 2×2 surfaces: a) pure CeO_2(111), b) (Ce,Zr^8)O_2(111). The top views only show the atoms in TL1. c) Top view of the relaxed TL2 trilayer and side view of (Ce,Zr^{13})O_2(111). The top view only shows the atoms in TL2. Relevant Zr-O and Ce-O bond lengths (in pm) are indicated. The atom color code is the same as in Figure 1, and Zr atoms are blue.

This is the version submitted to jpc c on october 7, 2019

As mentioned above, the preference of Zr for the subsurface rather than the surface layer relates to the preferred 8-fold coordination of Zr atoms in the cubic structure. Moreover, expectedly, the average Zr–O bond distances for Zr atoms at the surface and in deeper layers of the (Ce,Zr)O_2(111) system, are smaller than the corresponding Ce–O ones in pure CeO_2. As previously reported in the literature [16-18], a Zr dopant pulls the oxygen atoms in its neighborhood closer to itself and increases the O–Ce distances. Here, changes in the average Zr–O and Zr–Ce distances up to the third coordination spheres of the Zr dopants were investigated using the example of the 2×2 structures with one Zr atom (0.25 ML), in either TL1 (Zr^8), TL2 (Zr^{13}) or TL3 (Zr^{19}). Figure 4a-c shows selected bond lengths in the relaxed (111) surface of pure CeO_2 as well as of CeO_2 doped with a Zr in TL1 (Zr^8) and TL2 (Zr^{13}), with 2×2 periodicity. The first coordination sphere for Zr^8 in TL1 (Figure 4b) consists of seven oxygen anions with Zr^8-O bond distances of $1 \times 212 + 3 \times 213 + 3 \times 247$ pm, which yields an average bond length of 227 pm. For the Zr^{13} in TL2 (Figure 4c), the eight Zr^{13}-O bond distances in the first coordination shell are $3 \times 226 + 3 \times 232 + 1 \times 230 + 1 \times 222$ pm, i.e., an average Zr^{13}-O bond length of 228 pm, whereas for Zr^{19} in TL3, the corresponding average Zr^{19}-O bond length is 229 pm. Compared to the corresponding numbers for Ce atoms in TL1 (237 pm), TL2 (237 pm), and TL3 (237 pm) in the pure CeO_2 (111) surface (Figure 4a), the average Zr^8–O, Zr^{13}–O and Zr^{19}–O bond lengths are by 10, 9, and 8 pm smaller, respectively. These results are expected since the experimentally determined average Zr–O bond lengths in the low-temperature monoclinic (216 pm, [50]) and high-temperature tetragonal (226 pm, [51]), and cubic (227 pm, [52]) ZrO_2 bulk structures, in which Zr is 7-, 8-, and 8-fold coordinated, respectively, are smaller by 7 to 18 pm than the Ce–O bond length in bulk CeO_2 (234 pm, [53,54]). Thus, the closest environment of a Zr atom in the CeO_2 matrix is modified in such a way that the Zr-O bond distances become closer to that in ZrO_2. Furthermore, for the Ce (O) atoms in the second (third) coordination shell of Zr, the average Zr–Ce (Zr–O) distance is shortened by 2.3, 1.9, and 1.4 (2.9, 1.5, and 0.8) pm for Zr in TL1 (Zr^8), TL2 (Zr^{13}), and TL3 (Zr^{19}), respectively, as compared to their corresponding values in the undoped surface (see Table S2). In summary, the atomic displacements are largest for Zr in the surface layer. This result can be correlated with the larger energy gained from structural relaxation in the presence of Zr in TL1 (Zr^8), as compared to TL2 (Zr^{13}) or TL3, which results in the lowering of the surface energy by 0.253, 0.129, and 0.148 J/m^2, respectively (Table S1, 2×2 structures).

This is the version submitted to jpc c on october 7, 2019

3.2 Effect of Zr on the Energy of Oxygen Vacancy Formation

To study the formation of near-surface oxygen vacancies at the (Ce,Zr)O_2(111) surface, a 2×2 cell was used with one vacancy in the outermost oxygen layer or in the layer beneath. Hereinafter, V^A_{nm} (V^B_{nm}) is used to generally refer to a surface V^A (subsurface V^B) vacancy located in TL1, where the pair of sub-indices *n* and *m* (*m* ≥ *n*) is used to indicate the neighboring cationic coordination shells, respect to the oxygen vacancy, in which the two excess electrons (Ce^{3+}) are located (underlined $\underline{n}$ and $\underline{m}$ are in TL2). Figure 5 shows the calculated oxygen vacancy formation energy, E_f (eq 2), for all considered structures in which the Zr atom is placed in either TL1 (Zr^8) or TL2 (Zr^{13}), and the oxygen vacancy is located at the surface (V^A) or in the subsurface (V^B) within TL1, using the V^A_{nm} (V^B_{nm}) labeling, respectively. Detailed information on all considered structures is listed in the Supporting Information (Table S3), where a more detailed notation is also used to uniquely characterized the structures in which the specific location of the vacancy and the two Ce^{3+} is indicated, since for example, the configurations Zr^8–$V^{11}_{5,\underline{14}}$, Zr^8–$V^{10}_{7,\underline{13}}$, and Zr^8–$V^{12}_{6,\underline{16}}$ are all of the Zr^8–$V^B_{2,\underline{2}}$ type (cf. Figure 1c where atoms are labeled by number).

For Zr^8 in TL1, oxygen atoms have been removed so that both surface V^A and subsurface V^B vacancies are within the first anionic coordination sphere of the dopant (cf. O^1, O^2 or O^4, and O^{10}, O^{11} or O^{12} in Figure 1c, respectively). For Zr^{13} in TL2, surface V^A vacancies are within its second or third anionic coordination sphere (cf. O^3 and O^2, respectively), whereas subsurface V^B vacancies are either within its first or second coordination sphere (cf. O^{12} and O^9 in Figure 1c, respectively). As for the two excess electrons, they are located at different Ce sites at varying distances to the oxygen vacancies.

This is the version submitted to jpc c on october 7, 2019

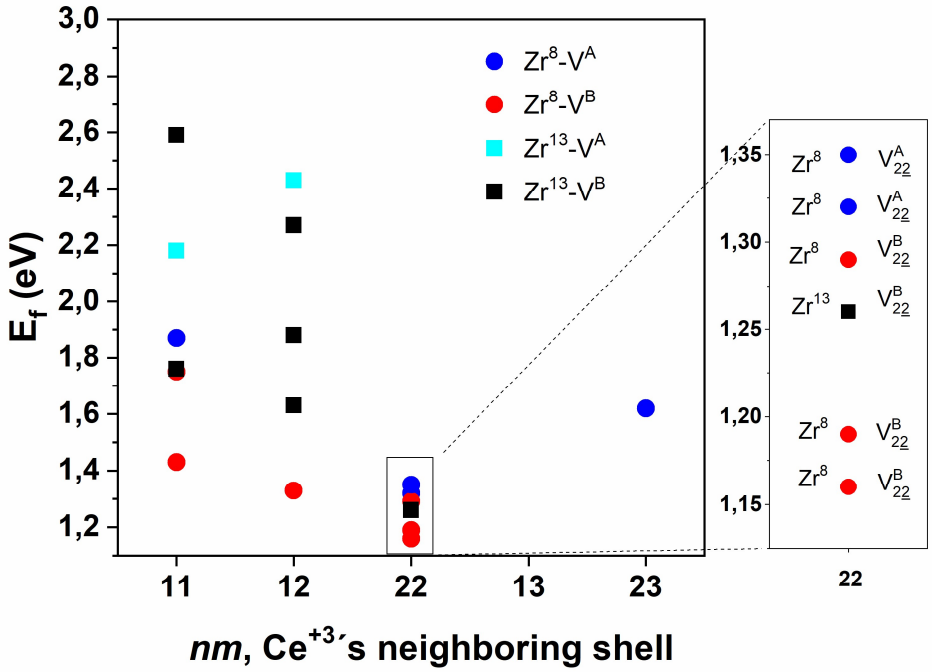

Figure 5: Near-surface oxygen vacancy formation energy at the (Ce,Zr)O_2(111) surface, E_f (eq 2),for several configurations with respect to the locations of the Zr dopant, the vacancy, and the associated Ce^{3+}. The structures are labeled $Zr^{8/13}$- $V^{A/B}{}_{nm}$, where $Zr^{8/13}$ denote the dopant location (cf. Figure 1), $V^{A/B}$ the vacancy location, and the sub-indices *n* and *m* denote the neighboring cationic coordination shells in which the two Ce^{3+} are located (see text). The red (blue) circles correspond to structures with a Zr^8 and a V^B (V^A) oxygen vacancy. The black squares correspond to structures with a Zr^{13} and a V^B oxygen vacancy, as close as possible to the Zr atom, and light blue symbols to configurations with a Zr^{13} and a V^A oxygen vacancy.

The E_f values obtained for the formation of a single oxygen vacancy with Zr in either TL1 or TL2, vary from 1.16 eV to 2.59 eV as shown in Figure 5 (cf. Table S3). Differences in the oxygen vacancy formation energy arise from the combined effect of having the Zr dopant, the oxygen vacancy, and the Ce^{3+} ions at different sites, but also surface lattice relaxations following vacancy formation play an important role, as will be discussed later in this work. The lowest E_f value of 1.16 eV corresponds to a Zr^8 and a V^B subsurface oxygen vacancy (O^{11}, cf. Figure 1c) with the two excess electrons localized at two next-nearest neighbor Ce ions, i.e, a $V^B{}_{2\underline{2}}$ ($V^{11}{}_{5,\underline{14}}$) configuration, with one Ce^{3+} in TL1 (Ce^5, cf. Figure 1c) and the other one in TL2 (Ce^{14}), and Ce^{3+}-Zr^8 distances equal to 3.83 and 5.30 Å, respectively (cf. Table S3); this structure will be discussed in more detail in the next section. The next lowest value, 1.19 eV, also corresponds to a Zr^8-$V^B{}_{2\underline{2}}$ structure ($V^{12}{}_{6,\underline{16}}$) with the Ce^{3+}-Zr^8 distances equal to 3.86 (Ce^6, cf. Figure 1) and 3.75 (Ce^{16}) Å. Noteworthy, the lowest oxygen vacancy formation energy values correspond to configurations with the Zr atom in TL1 (Zr^8) and the oxygen vacancy in the subsurface (Figure 5). This calls the attention because, as discussed in section 3.1 above, in the non-reduced (Ce,Zr)O_2(111) surface, the

smallest changes in the surface energy are obtained for Zr in TL2 or in deeper trilayers, but is in line with the suggestion of Mayernick and Janik [25] that in an oxidizing atmosphere, Zr atoms may prefer to remain in bulk-like layers of Zr-substituted CeO_2 surfaces, whereas in a reducing environment, Zr may prefer to segregate to the surface.

Other defect structures with low values of vacancy formation energy within the $1.26 \leq E_f \leq 1.35$ eV range (cf. Figure 5 and Table S3), correspond to a Zr^8 with a surface oxygen vacancy $V^A{}_{2\underline{2}}$ ($V^1{}_{5,\underline{14}}$, 1.32 eV and $V^1{}_{5,\underline{13}}$, 1.35 eV) or with a subsurface $V^B{}_{1\underline{2}}$ ($V^{11}{}_{5,\underline{16}}$, 1.33 eV) one, and to a Zr^{13} with a subsurface $V^B{}_{2\underline{2}}$ ($V^{12}{}_{6,\underline{15}}$, 1.26 eV) oxygen vacancy. We note that an initial structure with a Zr^8 and a $V^A{}_{1\underline{2}}$ ($V^2{}_{7,\underline{13}}$) oxygen vacancy, was found to be unstable; the oxygen vacancy initially located at the surface oxygen site O^2 (cf. Figure 1c), migrates towards the subsurface occupying the O^{10} oxygen site, resulting in a $V^B{}_{2\underline{2}}$ ($V^{10}{}_{7,\underline{13}}$) final configuration with a formation energy of 1.29 eV (Table S3). This value is by 0.1 eV slightly larger than that obtained for the equivalent $V^B{}_{2\underline{2}}$ ($V^{12}{}_{6,\underline{16}}$) configuration described above (E_f = 1.19 eV), which suggests that the final state after the migration of the oxygen vacancy, corresponds to a local minimum. Moreover, we note that for an additional number of initial structures with a Zr^8 or Zr^{13} and a surface vacancy, a migration of the vacancy to the subsurface has been observed (Table S3), which is already indicative of the higher stability of the subsurface vacancies in the doped surfaces.

Table 1. Lowest oxygen vacancy formation energy values, E_f (eV), for a surface (V^A) and subsurface (V^B) oxygen vacancy in CeO_2, $(Ce,Zr^8)O_2$ and $(Ce,Zr^{13})O_2(111)$ surfaces [2×2 periodicity], with the excess electrons localized at nearest or next-nearest Ce ions to the oxygen vacancy.

Oxygen vacancy	CeO_2 n =1, m =1[a]	CeO_2 n =2, m =$\underline{2}$	$(Ce,Zr^8)O_2$ n =1, m =1	$(Ce,Zr^8)O_2$ n =2, m =$\underline{2}$	$(Ce,Zr^{13})O_2$ n =1, m =1	$(Ce,Zr^{13})O_2$ n =2, m =$\underline{2}$[b]
V^A	2.52	2.24	1.87	1.32	2.18	–
V^B	2.38	1.89	1.75	1.16	1.76	1.26

[a]The sub-indices n and m denote the neighboring cationic coordination shells in which the two excess electrons are located (see text).
[b]Configurations with a Zr^{13}, a V^A oxygen vacancy, and two Ce^{3+} at next-nearest neighbor sites of the oxygen vacancy were found to be unstable.

Table 1 compares the lowest formation energies values for near-surface oxygen vacancies at the $(Ce,Zr)O_2(111)$ surface with Zr either in TL1 or TL2 and the excess electrons localized either in the first or second coordination sphere of the vacant oxygen site with the corresponding ones for the undoped surface. Inspection of Table 1 reveals that the more facile reduction for both the undoped and the doped surfaces, corresponds to the formation of subsurface oxygen vacancies (V^B) with the excess charge localized at next-nearest neighbor Ce sites (n=m=2), and

that the effect of Zr doping is substantial, resulting in systematically lower E_f values. As mentioned in the Introduction, the latter effect has been previously reported for the $(Ce,Zr)O_2(111)$ surface with Zr in TL1 and a V^A_{11} surface vacancy, [17,18,24,25] with lowerings of E_f in the 0.5 to 1.1 eV energy range.

Table 2. Oxygen vacancy formation energy, E_f (eV), for vacancies in bulk $(Ce,Zr)O_2$ or at the $(Ce,Zr)O_2(111)$ surface obtained by different methods, Zr content, cationic coordination shell of Zr in which the vacancy is located (Zr–V), and cationic coordination shell of the vacancy in which the Ce^{3+} are located (n,m), as reported in the literature.

Method	Cell	System	Zr content[d]	E_f	Zr–V	Ce^{3+} n,m	Ref.
DFT+U (PBE, U=6 eV)	$Ce_{32}O_{64}$	bulk[a]	0.03	2.38	1	1,1	16
DFT+U (PBE, U=5 eV)	$Ce_{16}O_{32}$ (2×2)	(111)[b]	1	2.35	1	1,1	17
				2.78	2	1,1	
DFT+U (LDA, U=5.5 eV)	$Ce_{27}O_{54}$ (3×3)	(111)[c]	0.11	2.20	1	1,1	18
				2.99	>>2		
DFT+U (PW91, U=6.3 eV)	Ce_8O_{16}	bulk[a]	0.125	2.03	1	1,1	19
			0.25	1.23			
			0.375	1.21			
			0.5	0.98			
			0.625	1.20			
			0.75	1.77			
			0.875	4.27			
DFT+U (PBE, U=4.5 eV)	$Ce_{32}O_{64}$	bulk[c]	0.03	2.57	1	1,1	20
DFT+U (PW91, U = 5 eV)	Ce_4O_8	bulk[a]	0.25	3.34[e]	1	1,1	23
			0.5	3.10[e]			
			0.75	4.45[e]			
DFT+U (PW91, U=5 eV)	$Ce_{24}O_{48}$ 2√3×3	(111)[c]	0.083	2.30	1	1,1	24
DFT+U (PW91, U=5 eV)	$Ce_{32}O_{64}$	bulk[c]	0.03	2.96	1	1,1	25,26
	$Ce_{16}O_{32}$ (2×2)	(111)[c]	0.25	1.63	1	1,1	
				2.61	2	1,1	

[a]Optimized cubic cell.
[b](2×2) surface unit cells with 4TL fixed at the calculated lattice parameters for cubic $Ce_{0.75}Zr_{0.25}O_2$ bulk and contains 1 Zr in each cationic plane.
[c]Lattice parameters for the undoped bulk are used to construct the doped bulk and surface models. In Ref. [24], the lattice parameters of the Zr-doped surface model were optimized.
[d]For the doped $CeO_2(111)$ surfaces, the Zr concentration (ML) is defined as the ratio between the actual number of Zr atoms in the supercell and the number of Zr atoms needed to fully dope one cationic layer within that cell.
[e]Values read from Figure 2 in Ref. [23].

Before rationalizing these findings in sec 3.3, especially considering the effect of Zr- and vacancy-induced lattice relaxation effects, in Table 2 we provide a brief overview of theoretical studies that have considered the formation of oxygen vacancies in Zr-doped bulk ceria or its (111) surface using a similar methodology –but not identical– than the one used in this work

[16-20,23-26]. Most reported studies have either found or presumed a localization of the excess charge at nearest neighbor Ce sites to the vacancy. Moreover, generally, vacancies were created within the first neighboring cationic shell of the dopant. However, in the cases in which a larger separation between dopant and vacancy has been considered [18,26], the calculated values indicate that vacancy creation within the first neighboring cationic shell of the dopant, is energetically preferred. As for the case of a surface vacancy (V^A) neighboring the Zr-dopant in TL1, and with the reduced Ce^{3+} cations within the first coordination shell of the vacant site (*n*=*m*=1), the predicted values lie within the 1.63−2.35 eV (Tables 1 and 2). Particularly due to the different unit cells, Zr content, and density functionals used, results cannot be directly compared. Specifically, Mayernick and Janik [25] reported a vacancy formation energy of 1.63 eV using a 2×2 cell (0.25 ML) and employing the DFT+U (PW91, U=5 eV) methodology, and thus the result may be compared to the one obtained in this work for the $(Ce,Zr^8)O_2$(111) surface, with V^A and *n*=*m*=1 (Table 1), namely, 1.87 eV (PBE, U=4.5 eV). The origin of this discrepancy is probably in the subtle computational details. To fully understand the fairly large discrepancies would require a very laborious testing of the separate effects of a considerable number of technical parameters on the calculated energies.

3.3 Lattice Relaxation Following Vacancy Formation

A. *Unrelaxed Structures*

In the following, we address the role of lattice relaxations upon oxygen removal on the energy of vacancy formation by considering first the creation of defects without allowing the lattice to relax. In such unrelaxed structures, the excess electrons are distributed practically homogeneously among the nearest neighbor Ce atoms to the oxygen vacancies. In Table 3 we compare the $E_f^{unrelax}$ (eq 2) values for the unrelaxed structures obtained after creating a surface (V^A) or a subsurface (V^B) oxygen vacancy with a Zr^8 (TL1) or a Zr^{13} (TL2), where the V^A vacancies are first neighbors of Zr^8 and second neighbors of Zr^{13}, and the V^B ones are first neighbors of both dopants (2×2 unit cell). Systematically, the $E_f^{unrelax}$ values for the V^B subsurface oxygen vacancies are higher than those for the V^A surface ones. Moreover, as a consequence of the presence of a Zr dopant in either TL1 (Zr^8) or TL2 (Zr^{13}), the $E_f^{unrelax}$ values for both vacancy types are lowered (cf. Table 3).

We first address the issue of why the $E_f^{unrelax}$ values for the V^B subsurface oxygen vacancies are higher than those for the V^A surface ones for both the undoped and doped surfaces. The creation of V^A and V^B vacancies implies the cutting of three and four bonds, respectively. The bond lengths of a given oxygen atom to its nearest neighbor cations in the (111) surface of pure CeO_2,

as well as of CeO_2 doped with Zr^8 or Zr^{13}, are shown in Figure 4. Not unexpected, the energy required to create unrelaxed surface and subsurface oxygen defects at the undoped CeO_2(111) surface by cutting three and four O–Ce bonds, respectively, with an average bond length of 237 pm, is largest for the subsurface vacancy by 0.15 eV (cf. 3.81 and 3.96 eV, Table 3) [36]. The same argument applies to the higher stability of the unrelaxed surface vacancy structures as compared to the subsurface ones in the presence of a Zr dopant (Table 3). For example, for a Zr dopant in TL1 (Zr^8), three and four O-(Ce/Zr) bonds of comparable average bond lengths must be cut to create a surface (236 pm, Figure 4b) and subsurface (235 pm) vacancy, respectively, and the vacancy formation energy is largest for the latter by 0.29 eV (cf. 3.17 and 3.46 eV, Table 3).

Table 3: Unrelax vacancy formation energy, $E_f^{unrelax}$ (eV), for a surface vacancy (V^A) and a subsurface vacancy (V^B) with Zr in the TL1 (Zr^8), TL2 (Zr^{13}), and TL3 (Zr^{19}) trilayers.

$(Ce,Zr)O_2$	**$E_f^{Unrelax}$**	
	Surface Vacancy (V^A)	**Subsurface Vacancy (V^B)**
Clean	3.81	3.96
Zr^8	3.17	3.46
Zr^{13}	3.42	3.76
Zr^{19}	3.88	3.95

In the following paragraphs, we address the issue of why the $E_f^{unrelax}$ values for both vacancy types are lower for the surfaces with Zr in the near-surface region, as compared to the undoped one. As discussed above (Section 3.1), a Zr dopant perturbs the lattice, especially in its vicinity. The asymmetry observed for the O-(Ce/Zr) bonds distances for O at the surface and in the subsurface, particularly the significant lengthening of O–Ce bonds, is behind the lowering of the energy cost to create both unrelaxed vacancy structures as compared to CeO_2(111). Here, we explicitly consider the example of the perturbations induced by a Zr^8 dopant in TL1 from the point of view of the three-fold and four-fold coordinated oxygen atoms at the surface or in the subsurface, respectively, which would be removed to create neutral oxygen vacancies neighboring the Zr dopant. In the presence of a Zr^8 dopant in TL1, for a three-fold coordinated nearest oxygen atom at the surface, the one O-Zr bond (213 pm) is comparatively shorter by 24 pm than the corresponding O–Ce bond (237 pm) in the undoped surface (cf. Figures 4a and 4b), but the two O-Ce bonds (248 pm) are noticeably longer by 11 pm. Hence, the surface oxygen is more labile in the doped system, resulting in the lowering of the energy cost to create the (unrelaxed) surface oxygen vacancy by 0.64 eV, as compared to the undoped surface (cf. 3.81 and 3.17 eV, Table 3). Similarly, a four-fold coordinated nearest neighbor subsurface oxygen

atom to the Zr^{8} dopant has two bonds to Ce in TL1 (232 pm) and one to Ce in TL2 (228 pm), which are somewhat shorter by 6 pm than the corresponding ones in the pure surface (cf. Figure 4a and 4b), but one noticeably long O-Zr^{8} bond of 247 pm, resulting also in the lowering of the energy cost to create the (unrelaxed) subsurface vacancy by 0.50 eV, as compared to the undoped surface (cf. 3.96 and 3.46 eV, Table 3). A similar analysis can be performed for a Zr^{13} in TL2, whose presence also decreases the energy needed to form surface or subsurface oxygen vacancies, but to a lesser extent when compared to the effect that a Zr^{8} in TL1 has (cf. Table 3). This correlates with the less noticeable effect on the lengths of the O-(Ce/Zr) bonds that must be cut to create the near-surface vacancies. For example, the closest subsurface O atom to Zr^{13} has three slightly elongated O-Ce bonds (239 pm) and one shorter O-Zr bond (222pm), as compared to the corresponding ones in pure CeO_2 (3× 238 pm, 1× 234 pm, cf. Figures 3a and 3c). Furthermore, the same calculations carried out with a Zr in the third trilayer (Zr^{19}) yield an energy formation for an unrelaxed surface vacancy of 3.88 eV, a value close to that obtained for pure CeO_2 (cf. Table 3) indicating a short range effect of the Zr dopant on the energy of a surface oxygen vacancy formation, as discussed by Hu and Metiu [18]. A similar behavior is observed in the case of the subsurface oxygen vacancy (cf. Table 3), as the Zr dopant moves from TL1 to TL3, the unrelaxed oxygen vacancy formation energy varies according the sequence 3.46 → 3.76 → 3.95 eV, being the last value comparable to the value obtained for pure CeO_2.

In summary, if lattice relaxations upon oxygen vacancy formation in the near-surface of (Ce,Zr)O_2(111) are *not* allowed, a surface vacancy is more stable than a subsurface one, and Zr doping facilitates the formation of both types of vacancies, with its effect becoming less and less noticeable with the increase of the distance between the dopant and the near-surface (Table 3). However, inspection of Table 1 reveals that lattice relaxations, which are accompanied by the localization of the excess charge, change the relative stability of surface and subsurface vacancies, and it is also observed that the excess electrons preferably localize at Ce cations which are next-nearest neighbors to the vacancies. These effects will be discussed in more detail in the following section.

B. *Relaxed Structures, Excess Charge Localization, and Subsurface Preference*

B.1 Surface and subsurface vacancy formation energy with Zr in TL1

The creation of an unrelaxed surface oxygen vacancy (V^{A}) in pure CeO_2 (111) costs $E_f^{unrelax} =$ 3.81 eV (cf. Table 3). However, after allowing for lattice relaxation and, if the excess electrons are localized in nearest neighbor Ce sites to the vacancy ($V^{A}{}_{11}$), it costs $E_f = 2.52$ eV (Table 1),

This is the version submitted to jpc c on october 7, 2019

i.e., a decrease of $E_f^{relax} = 1.29$ eV (cf. eq 2), in agreement with previous works [36,38]. Moreover, the localization of the excess charge at next-nearest neighbor Ce atoms ($V^A{}_{22}$), further stabilizes the vacancy by 0.28 eV, i.e., the lowest energy cost to create a surface vacancy in pure CeO_2(111) is $E_f = 2.24$ eV, in line with work in the literature [36,38,39]. The mere incorporation of a Zr^8 atom in the CeO_2(111) surface (TL1) results in the lowering of the unrelaxed surface vacancy formation energy by 0.64 eV (from 3.81 to 3.17 eV, Table 3), as discussed above. When the surface is allowed to relax, in the case in which the excess charge is localized in nearest neighbor Ce sites to the vacancy ($V^A{}_{11}$), the vacancy is stabilized by $E_f^{relax} = 1.30$ eV (cf. 1.87 eV, Table 1). However, if the excess electrons are localized at two next-nearest neighbor Ce atoms ($V^A{}_{22}$), the vacancy is further stabilized by an extra energy gain of 0.55 eV (cf. 1.32 eV, Table 1). In summary, the comparison with pure CeO_2 shows that the presence of Zr^8 reduces the cost to create an unrelaxed surface vacancy by 0.64 eV, from 3.81 to 3.17 eV (Table 3), and a relaxed $V^A{}_{22}$ one by 0.92 eV, from 2.24 to 1.32 eV (Table 1).

As for the creation of an unrelaxed subsurface oxygen vacancy (V^B), it is by 0.5 eV more facile in the doped (Ce,Zr^8)O_2 (111) surface than in the undoped one (cf. 3.46 and 3.96 eV, respectively, Table 3), as described above. When lattice relaxation in the presence of the subsurface oxygen vacancy is allowed, if the excess electrons are localized at two nearest neighbor Ce sites to the vacancy ($V^B{}_{11}$), the vacancy formation energy in (Ce,Zr^8)O_2(111) is $E_f = 1.75$ eV (Table 1), that means an extra stabilization of $E_f^{relax} = 1.71$ eV [cf. 3.46 and 1.75, Tables 3 and 1, respectively]. However, if the two excess electrons are localized at two next nearest Ce atoms ($V^B{}_{22}$), the subsurface oxygen vacancy formation energy further decreases up to 1.16 eV (Table 1) i.e., an additional energy gain of 0.59 eV is obtained (cf. 1.75 and 1.16 eV for $V^B{}_{11}$ and $V^B{}_{22}$, respectively, Table 1). Compared to the results for the formation of a subsurface oxygen vacancy in the undoped CeO_2(111) surface (Table 1), the presence of Zr^8 reduces the cost to create a relaxed $V^B{}_{22}$ subsurface vacancy by 0.73 eV, from 1.89 to 1.16 eV.

As anticipated above, it is only when the energy gained from lattice relaxations (E_f^{relax}, eq 2) is considered that the preference for subsurface oxygen vacancy formation in the (Ce,Zr^8)O_2(111) system can be explained. The creation of unrelaxed vacancies in the near-surface favors the surface vacancy by [$E_f^{unrelax}$ (V^B)–$E_f^{unrelax}$(V^A)] = 0.29 eV (Table 3). Adding the amount by which both the energy of a $V^A{}_{22}$ surface and a $V^B{}_{22}$ subsurface vacancy formation are lowered due to lattice relaxations, i.e., E_f^{relax}($V^A{}_{22}$) = 1.85 and E_f^{relax}($V^B{}_{22}$)= 2.30 eV, respectively (cf. Tables 1 and 3), results in the preference for subsurface oxygen vacancy formation by 0.16 eV {[$E_f^{unrelax}$ (V^B)–E_f^{relax}($V^B{}_{22}$)]– [$E_f^{unrelax}$(V^A)–E_f^{relax}($V^A{}_{22}$)]}. In the following sections 3.3.B.2 and 3.3.B.3, the vacancy induced lattice relaxation effects will be discussed in detail.

B.2. Surface oxygen vacancy lattice relaxation with Zr in TL1

An important contributing factor to the lattice relaxation upon oxygen removal is the electrostatic interaction between the positive charged oxygen vacancy and its neighboring ions, resulting in the closest cations moving away from the oxygen vacant site and the anions toward it. Figure 6 shows the directions of the displacement vectors of the neighboring ions to a $V^{A}_{2\underline{2}}$ surface vacancy at the undoped and doped surfaces with Zr in TL1 (Zr^{8}). For pure CeO_2 (CeO_2-$V^{3}_{8,\underline{16}}$), the first neighbor Ce^{4+} cations in TL1 of the vacancy, and the closest O atoms in the subsurface (O^{10}, O^{11} and O^{12}), are displaced an average distance of 16 and 48 pm, respectively (Figures 6a-b). Moreover, the six surface oxygen atoms ($2\times O^{1}$, $2\times O^{2}$ and $2\times O^{4}$) close to the $V^{A}_{2\underline{2}}$ oxygen vacancy, forming a hexagon, relax perpendicular to the surface an average of 10 pm, similar to the values reported in the literature [30,36].

When a $V^{A}_{2\underline{2}}$ surface oxygen vacancy is created at the (Ce,Zr^{8})O_2(111) surface (Zr^{8}-$V^{1}_{5,\underline{14}}$) (Figures 6c-d), the average displacement of the closest subsurface oxygen ions towards the vacancy increases to about 58 pm (O^{9}, O^{10} and O^{12} by 42, 66 and 67 pm, respectively), i.e., it is approximately 10 pm larger than in pure CeO_2. Moreover, the average perpendicular displacement of the six neighboring surface oxygen atoms ($2\times O^{2}$, $2\times O^{3}$ and $2\times O^{4}$) is also increased by 5 pm, as compared to pure CeO_2.

Regarding the closest cations to the $V^{A}_{2\underline{2}}$ vacancy in TL1, they move an average distance of about 18 pm, which is close to the average distance of 16 pm that Ce cations move in pure CeO_2, however, the actual displacements of the Zr^{8} and the two Ce cations neighboring the vacancy are by 14 pm larger and between 4 and 5 pm smaller, respectively, than the corresponding ones in the undoped system (cf. Figures 6b-d). Moreover, compared to the Zr^{8}–O distance of 213 pm (Figure 4b) in the unreduced (Ce,Zr^{8})O_2(111) system, upon oxygen removal, the Zr^{8}– $V^{A}_{2\underline{2}}$ distance is elongated by approximately 30 pm (cf. Figure 6d and Table S3). This effect of the Zr^{8} pulling away from the oxygen vacancy was also observed by Hu and Metiu [18]. Furthermore, Zr^{8} takes advantage of the presence of the surface vacancy to change its initial 7-fold coordination (3×213; 3×247; 1×212) with an average bond length of 228 pm (cf. Figure 4b) to a 6-fold one (1×214; 1×215; 1×212 ;1×218; 1×219; 1×209) with an average bong length of 215pm, which is closer to the average bond distance of Zr in the low-temperature monoclinic crystal structure (216 pm [51]), although in this case Zr is coordinated by 7 oxygen atoms and the dispersion of the Zr-O bond lengths is larger.

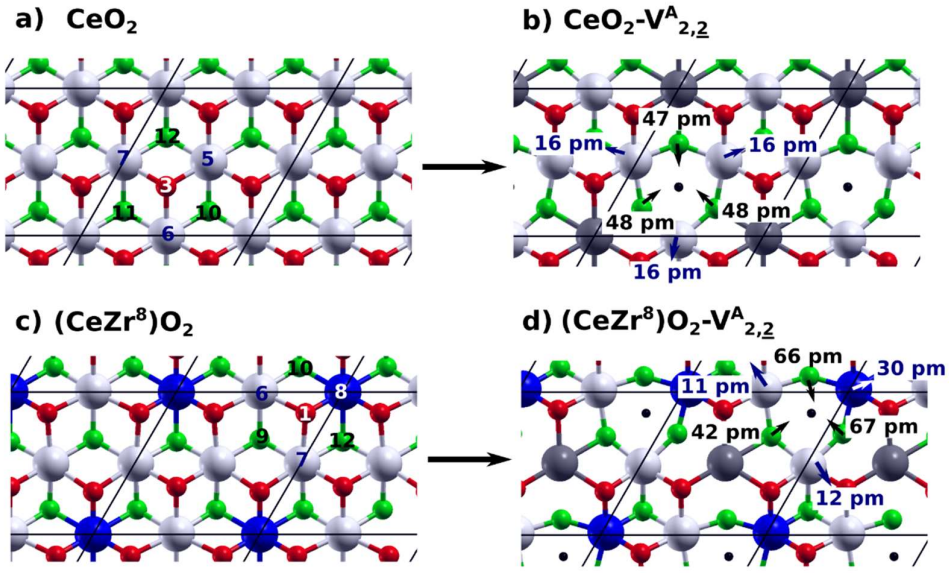

Figure 6. Top view of the first trilayer (TL1) of a-b) the CeO_2(111) and c-d) the $(Ce,Zr^8)O_2$(111) surface before and after the formation of a surface oxygen vacancy ($V^A_{2,2}$, namely, $V^3_{8,16}$ and $V^1_{5,14}$ for CeO_2 and $(Ce,Zr^8)O_2$, respectively, cf. Figure 1 for sites labeling). The arrows indicate the direction of the displacements upon vacancy formation of the atoms surrounding the vacancy which is marked with a black point. The displacements are indicated in pm. The atom color code is the same as in Figure 1, and Zr^{4+} and Ce^{3+} ions are depicted blue and dark grey, respectively; the latter are located in next-nearest neighbor Ce sites to the vacancy.

B.3. Subsurface oxygen vacancy lattice relaxation with Zr in TL1

For the case of the $V^B_{2,2}$ subsurface oxygen vacancies in the pure CeO_2 and $(Ce,Zr^8)O_2$(111) surfaces, the relaxed structures are displayed in Figures 7a-b and 7c-d, respectively. As expected, also for subsurface vacancies, the closest cations and anions to the vacancy move away from and toward the vacant site, respectively. In the $(Ce,Zr^8)O_2$(111) system with a subsurface vacancy (Zr^8-$V^{11}_{5,14}$), the neighboring O atoms in TL1, i.e., O^3, O^2 and O^4, moved by 23, 30 and 55 pm (Figure 7d), respectively, whereas those in TL2 moved by 24, 27 and 36 pm, giving an average of 32.5 pm. In this case, O^4 becomes the closest surface oxygen atom to the vacancy, whereas O^3, the only surface oxygen that is not linked to the Zr^8, is farthest. The surface oxygen atoms O^1, forming a triangle around the vacancy, move a total distance of 30 pm, mainly a displacement perpendicular to the surface of 28 pm. In comparison, for the CeO_2(111) surface with a $V^B_{2,2}$ vacancy ($V^{12}_{6,15}$, Figure 7b), the neighboring O atoms in TL1 (O^1, O^3 and O^4) moved 29 pm and those in TL2, 15 pm, and the farthest surface oxygen atoms (O^2) exhibit a perpendicular outward relaxation of 31 pm, in line with work in the literature [30, 36].

Moreover, in the $(Ce,Zr^{8})O_2(111)$ surface, the Zr and Ce cations surrounding the subsurface V^{B}_{22} vacancy move away from it by an average of about 17 pm (Zr^{8}, Ce^{7}, and Ce^{6} in TL1 by 15, 26 and 13 pm, respectively, and Ce^{16} in TL2 by 16 pm), whereas in the undoped surface, all neighboring Ce cations move away by 16 pm.

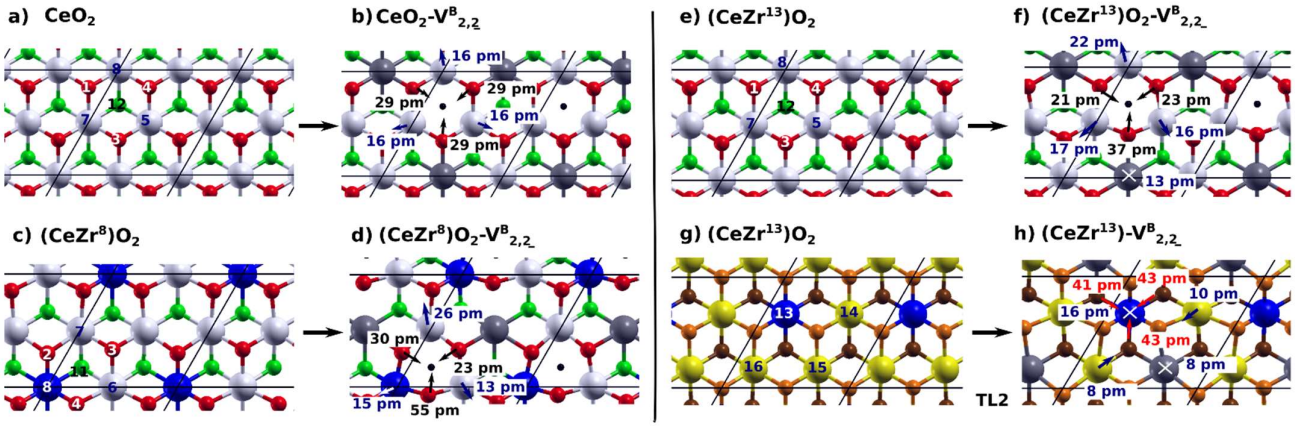

Figure 7. Top view of the first trilayer (TL1) of a-b) the $CeO_2(111)$ surface, c-d) the $(Ce,Zr^{8})O_2(111)$, and e-f) the $(Ce,Zr^{13})O_2(111)$ surface before and after the formation of a subsurface oxygen vacancy (V^{B}_{22}, namely, $V^{12}_{6,15}$, $V^{11}_{5,14}$ and $V^{12}_{6,15}$ for CeO_2, $(Ce,Zr^{8})O_2$ and $(Ce,Zr^{13})O_2$, respectively, cf. Figure 1 for sites labeling). g-h) Top view of the second trilayer (TL2) of the $(Ce,Zr^{13})O_2(111)$ surface without and with the V^{B}_{22} vacancy. The arrows indicate the direction and values of the displacements upon vacancy formation of the atoms surrounding the vacancy which is marked with a black point. The atom color code is the same as in Figure 1, and Zr^{4+} and Ce^{3+} ions are depicted blue and dark grey, respectively; the latter are located in next-nearest neighbor Ce sites to the vacancy.

Furthermore, the above-mentioned preference of the excess charge to localize at next-nearest neighbor cationic sites to the near-surface oxygen vacancies at the $(Ce,Zr^{8})O_2(111)$ surface is explained by the better ability of the system in such configurations to relax the lattice strain induced upon reduction while better accommodating the more spacious Ce^{3+} ions than their Ce^{4+} counterpart. For example, for the V^{A}_{22} configuration, the average Ce^{3+}-O bond lengths are 257 and 252 pm for the Ce^{3+} in TL1 and TL2, respectively, which are clearly larger than those in the V^{A}_{11} structure with a length of 242 pm (Table S4). Similar changes are observed when comparing the average Ce^{3+}-O bond lengths in the V^{B}_{22} and the V^{B}_{11} structures (Table S5). The larger Ce^{3+}-O bond lengths are comparable to the average experimental bond length of the 7-fold coordinated Ce^{3+} ions in Ce_2O_3, i.e., 251 pm [55]. Thus, the excess electrons prefer to localize at Ce sites where the Ce^{3+} ions are less compressed and therefore the energy gain from the lattice relaxations is largest in the V^{A}_{22} and V^{B}_{22} configurations. Such behavior is also found for near-surface oxygen vacancies when the dopant is in deeper layers such as TL2 (Zr^{13}) and TL3 (Zr^{19}), cf. Tables S4 and S5.

This is the version submitted to jpc c on october 7, 2019

B.4 Surface and subsurface vacancy formation energy with Zr in TL2

In the following, we briefly comment on the effect of having a nearby Zr dopant in TL2 [(Ce,Zr^{13})O_2(111)] on the formation energy of surface (V^A) and subsurface (V^B) oxygen vacancies, and compare to that of having the dopant in TL1 [(Ce,Zr^8)O_2(111)], discussed above. Inspection of Table 1 reveals that the presence of Zr in TL2 makes creating near-surface oxygen vacancies in (Ce,Zr)O_2(111) more difficult than when it is in TL1. To further discuss the details, the vacancy formation energy difference $\Delta E_f = [E_f(\mathrm{Zr}^{13}\text{-}\mathrm{V}^{A/B}) - E_f(\mathrm{Zr}^{8}\text{-}\mathrm{V}^{A/B})] = \Delta E_f^{unrelax} - \Delta E_f^{relax}$ is considered (cf. eq 2). The creation of unrelaxed surface and subsurface vacancies in (Ce,Zr^{13})O_2(111) costs 0.25 and 0.30 eV (ΔE_f^{unrela}) more, respectively, than in (Ce,Zr^8)O_2(111) [cf. 3.42 with 3.17 and 3.76 with 3.46 eV, respectively, Table 3]. As discussed above (sec 3.3.A), a Zr dopant in (Ce,Zr)O_2(111) induces changes in the O-(Ce/Zr) bonds distances that facilitate the creation of unrelaxed vacancy structures, as compared to pure CeO_2(111). These facilitating lattice perturbations upon doping are less noticeable in the (Ce,Zr^{13})O_2(111) system, as compared to (Ce,Zr^8)O_2(111), which correlates with the calculated $\Delta E_f^{unrelax} > 0$ values. If one takes into account the difference of the energies gained from lattice relaxations in the presence of the vacancies ($E_f^{relax} > 0$, $\Delta E_f^{relax} \gtrless 0$), the creation of near-surface oxygen vacancies still remains more facile in (Ce,Zr^8)O_2(111) than in (Ce,Zr^{13})O_2(111). For instance, the difference in the lattice relaxation energy gain when $V^B{}_{2\underline{2}}$ subsurface oxygen vacancies are created within the first coordination sphere of Zr^{13} and Zr^8 is $\Delta E_f^{relax} = [E_f^{relax}(\mathrm{Zr}^{13}\text{-}\mathrm{V}^B{}_{2\underline{2}}) - E_f^{relax}(\mathrm{Zr}^{8}\text{-}\mathrm{V}^B{}_{2\underline{2}})] = 2.50 - 2.30 = 0.20$ eV [cf. 3.76 with 1.26 and 3.46 with 1.16, Tables 3 and 1, and discussion in sec 3.3.B.5 below]. If one subtracts this difference from the corresponding one for the unrelaxed structures ($\Delta E_f^{unrelax} = 0.30$ eV), one obtains $\Delta E_f = 0.10$ eV, which is the amount by which a $V^B{}_{2\underline{2}}$ vacancy is more stable if the dopant is in TL1, as compared to when it is in TL2 (cf. 1.16 and 1.26 eV, Table 1).

The analysis of the near-surface vacancy structures with nearest neighbor Ce^{3+} sites, i.e., $V^A{}_{1\underline{1}}$ and $V^B{}_{1\underline{1}}$, respectively, in both (Ce,Zr^{13})O_2 and (Ce,Zr^8)O_2(111) systems points out that similar considerations apply as regards the higher stability of such vacancies when Zr is in TL1 (Tables 1 and 3). We note that in the case of a neighboring surface vacancy to Zr^{13} in TL2, a structure in which the two excess electrons were initially located at two next nearest Ce atoms, $V^A{}_{2\underline{2}}$, was found to be unstable, namely, the vacancy migrated to the subsurface in seeking to reach a more stable configuration. In the following section 3.3.B.5, the subsurface vacancy induced lattice relaxation effects in both (Ce,Zr^{13})O_2 and (Ce,Zr^8)O_2(111) systems will be discussed in detail.

B.5 Subsurface oxygen vacancy lattice relaxation with Zr in TL2

The lattice distortion in the case of a $V^{B}_{2\underline{2}}$ subsurface oxygen vacancy with Zr in TL2 [(Ce,Zr^{13})O_2(111)] is shown in Figures 7e-f. Also in this case, neighboring cations move away from the subsurface oxygen vacant site, and anions toward it. Specifically, Zr^{13}, Ce^{5}, Ce^{7}, and Ce^{8} moved by 16, 16, 17 and 22 pm, respectively, i.e., cations moved away from the vacancy by an average of about 18 pm, which is slightly more than when Zr is in TL1 [(Ce,Zr^{8})O_2(111)] (17 pm), as discussed above (sec 3.3.B.3). Moreover, the Zr^{13} movement is accompanied by the shortening of the Zr^{13}–O bonds with O in the third anionic plane in TL2, from 232 pm (cf. Figure 4c) to 2 × 216 and 1 × 217 pm. In this way, Zr^{13} changes its coordination from 8-fold, with an average bond length of 228 pm, to 7-fold, with average bond length of 221 pm, thereby resembling the 7-fold Zr coordination in the monoclinic phase, in which Zr binds to three oxygen atoms at 219, 216 and 215 pm, forming a triangle, as well as to other four ones with bond lengths of 2 × 205, 220 and 228 pm, forming a prism [50].

Furthermore, the neighboring surface oxygen atoms to the $V^{B}_{2\underline{2}}$ vacancy in (Ce,Zr^{13})O_2(111), i.e., O^{1}, O^{3} and O^{4}, moved toward the vacancy by 21, 37 and 23 pm, respectively, whereas the three oxygen atoms in TL2 moved 41, 43 and 43 pm, resulting in an average displacement of 35 pm (Figure 7d). In addition, the surface oxygen atoms forming a triangle around the vacancy, O^{2}, relaxed perpendicular to the surface by 28 pm. These oxygen movements are generally larger than those observed for the case of a $V^{B}_{2\underline{2}}$ vacancy in the (Ce,Zr^{8})O_2(111) surface (sec 3.3.B.3), which is in line with the above-mentioned larger relaxation energy gain of the Zr^{13}-$V^{B}_{2\underline{2}}$ configuration (2.50 eV) compared to the Zr^{8}-$V^{B}_{2\underline{2}}$ configuration (2.30 eV).

4. CONCLUSIONS

This work shows the important effect of Zr doping on the stability of both the oxidized (Ce,Zr)O_2(111) surface, and reduce one with near-surface oxygen vacancies, as compared to the corresponding undoped surface. By calculating the change in the surface energy upon Zr doping, we have found that the surface stability increases as Zr occupies cationic sites of inner O–Ce–O trilayers, which has been related to the preference of Zr^{4+} for the 8-fold coordination in the cubic (fluorite) structure. Moreover, a slight preference for the second cationic plane, as well no tendency to form zirconia aggregates, have been observed. For the example of a Zr concentration of 0.25 ML, the structure with Zr in the second cationic plane is by 0.17 eV more stable than that with Zr in the surface layer (cf. Figure 8).

Considering that ceria-doped sample preparation is usually performed in an oxidizing atmosphere like air, and the results of the surface energy calculations, it is expected that a large fraction of Zr dopants will exist in the inner surface of real samples. However, it is also possible

that depending on the sample preparation method, a non-homogeneous distribution of Zr is obtained. For example, if samples are prepared using a combustion method [13], dopants are likely not to have enough mobility to find the lowest energy site, and thus, the presence of Zr atoms at the surface is also expected.

We have further analyzed the effects of Zr doping on the energy cost to create near-surface oxygen vacancies, and the key results are summarized in Figure 8. We found that the most labile oxygen atoms are those in the subsurface, closest to a Zr dopant at the surface and with two next-nearest neighbor Ce^{3+} ions [$(Ce,Zr^{8})O_2$-V^{B}_{22}], whereas the corresponding oxygen vacancies at the surface are by 0.16 eV less stable [$(Ce,Zr^{8})O_2$-V^{A}_{22}]. Moreover, if Zr is in the second cationic plane [$(Ce,Zr^{13})O_2$-V^{B}_{22}], the subsurface vacancy is by 0.10 eV less stable than the lowest-energy vacancy structure, whereas the surface vacancy is not stable. Hence, if Zr dopants are present near the surface under reducing conditions, our predicted trend in the thermodynamic stability of near-surface oxygen vacancies is $(Ce,Zr^{8})O_2$-V^{B}_{22} > $(Ce,Zr^{13})O_2$-V^{B}_{22} > $(Ce,Zr^{8})O_2$-V^{A}_{22}. Furthermore, we confirmed the predicted local nature of the effect of Zr dopants on the energy cost to create near-surface oxygen vacancies [18].

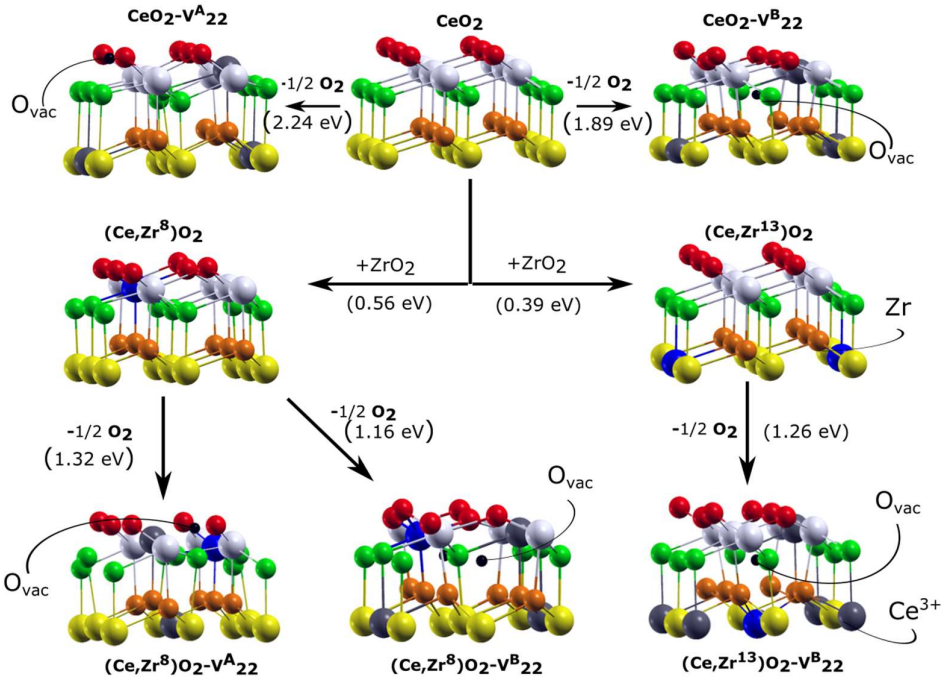

Figure 8. Side views of the oxidized CeO_2, $(Ce,Zr^{8})O_2$ and $(Ce,Zr^{13})O_2$(111) surfaces, as well as of the reduced structures with a surface (V^{A}_{22}) or a subsurface oxygen vacancy (V^{B}_{22}). Reaction energies are given in eV. The doping reaction energy is equal to $\Delta\Gamma * A$ (eq 1), and the vacancy formation energy is given by E_f (eq 2). For these calculations a four TL-thick (2×2) slab has been used (cf. Table S1).

This is the version submitted to jpc c on october 7, 2019

The preference of the oxygen vacancies for the subsurface sites of the doped reduced ceria surfaces has been explained as the result of the larger energy gain due to the lattice relaxations that accompany the removal of a neutral oxygen atom in the subsurface, as compared to an oxygen atom at the surface. This explanation is also valid for the preference of vacancies for subsurface sites in the pure ceria surface [36]. Similarly, for both the doped and undoped reduce surfaces, the Ce^{3+} preference for the next-nearest neighbor cationic sites to both surface and subsurface vacancies has been explained by the better ability of the systems to accommodate the lattice strain induced by the presence of the vacancies, as well as by the localization of the excess charge; a Ce^{3+} ion is more spacious than its Ce^{4+} counterpart and at nearest neighbor sites Ce^{3+}–O bonds would be compressed. This preference is more pronounced for the doped surfaces.

Finally, we found that Zr doping has an important effect on the actual energy cost to create near-surface oxygen vacancies at the CeO_2(111) surface. Zr doping results in an overall lowering of the vacancy formation energy with values that are lower by up to 0.9 eV than those obtained for the creation of the corresponding vacancies in the undoped surface (cf. Figure 8). Our calculations show that Zr in (Ce,Zr)O_2(111) induces changes in the O-(Ce/Zr) bonds distances that results into more labile oxygen atoms bonded to Zr, as compared to the corresponding atom in the undoped CeO_2(111) surface, which are then easier to remove. Moreover, lattice relaxation effects following oxygen removal are larger for the doped systems, which further stabilizes the vacancies in the presence of Zr dopants.

In catalytic applications, Zr doping is used to enhance the thermal stability and to increase oxygen release from ceria. Our results provide a microscopic understanding of the interplay between doping, vacancy formation, lattice relaxations, and the localization of the excess charge that will be key to understanding surface chemistry and catalysis on (Ce,Zr)O_2(111) surfaces.

ASSOCIATED CONTENT

Supporting Information

The Supporting Information is available free of charge on the ACS Publications website at DOI:

Table of calculated changes in the surface energy, $\Delta\Gamma$(J/m^2), as function of Zr concentration for different dopant configurations. Table of near-surface oxygen vacancy formation energies at the (Ce,Zr)O_2(111) surface, E_f(eV), for several configurations with respect to the locations of the Zr dopant, the vacancy, and the associated Ce^{3+}. Selected bond lengths are listed throughout the supporting material.

This is the version submitted to jpc c on october 7, 2019

AUTHOR INFORMATION

Corresponding Author

*E-mail: lustemberg@ifir-conicet.gov.ar

Notes

The authors declare no competing financial interest.

ACKNOWLEDGEMENTS

This work was supported by CONICET and ANPCyT, Argentina, through PIP 112 2013 0100151 CO and PICT 2016-1921 and 2014-1778, respectively. The authors also acknowledge the funding from Universidad Nacional del Sur through PGI24/F063 and 24/F070. This project has received funding from the European Union's Horizon 2020 research and innovation programme under the Marie Skłodowska-Curie grant agreement No 832121. Computer time provided by the BIFI-ZCAM, the RES resources at Marenostrum nodes, and the Piluso node within SNCAD (Sistema Nacional de Computación de Alto Desempeño, Arg), is acknowledged. M.V.G.P. thanks the support by the MINECO and MICINN-Spain (CTQ2015-71823-R and RTI2018-101604-B-I00, respectively).

REFERENCES

[1] Shelef, M.; McCabe, R. Twenty-five Years After Introduction of Automotive Catalysts: What Next? *Catal. Today* **2000**, *62*, 35-50.

[2] Montini, T.; Melchionna, M.; Monai, M.; Fornasiero, P. Fundamentals and Catalytic Applications of CeO_2-Based Materials. *Chem. Rev.* **2016**, *116*, 5987-6041.

[3] *Catalysis by Ceria and Related Materials*; Trovarelli, A.; Fornasiero, P., Eds.; 2nd Edition; Imperial College Press: London, 2013; and references therein.

[4] Kim, D. -J. Lattice Parameters, Ionic Conductivities, and Solubility Limits in Fluorite Structure MO_2 Oxide [M = Hf^{4+}, Zr^{4+}, Ce^{4+}, Th^{4+}, U^{4+}] Solid Solutions. *J. Am. Ceram. Soc.* **1989**, 72, 1415-1421.

[5] Farra, R.; Garcia-Melchor, M.; Eichelbaum, M.; Hashagen, M.; Frandsen, W.; Allan, J.; Girgsdies, F.; Szentmiklósi, L.; Lopez, N.; Teschner, D. Promoted Ceria: A Structural, Catalytic, and Computational Study. *ACS Catal.* **2013**, *3*, 2256-2268.

[6] Hedge, M.; Madras, G.; Patil, K. Noble Metal Ionic Catalysts. *Acc. Chem. Res.* **2009**, *42*, 704-712.

[7] Ozawa, M; Kimura, M.; Isogai, A. The Application of Ce-Zr Oxide Solid Solution to Oxygen Storage Promoters in Automotive Catalysts. *J. Alloys Compd.* **1993**, *193*, 73-75.

[8] Fornasiero, P.; Di Monte, R.; Ranga Rao, G.; Kaspar, J.; Meriani, S.; Trovarelli, A.; Graziani, M. Rh Loaded CeO_2-ZrO_2 Solid Solution as Highly Efficient Oxygen Exchangers: Dependence of the Reduction Behavior and the Oxygen Storage Capacity on the Structural Properties. *J. Catal.* **1995**, *151*, 168-177.

[9] Fornasiero, P.; Balducci, G.; Di Monte, R.; Kaspar, J.; Sergo, V.; Gubitosa, G.; Ferrero, A.; Graziani, M. Modification of the Redox Behaviour of CeO_2 Induced by Structural Doping with ZrO_2. *J. Catal.* **1996**, *164*, 173-183.

[10] Sun, Y.; Li, C.; Djerdj, I.; Khalid, O.; Cop, P.; Sann, J.; Weber, T.; Werner, S.; Turke, K.; Guo, Y.; Smarsly, B.; Over, H. Oxygen Storage Capacity versus Catalytic Activity of Ceria–Zirconia Solid Solutions in CO and HCl oxidation. *Catal. Sci. Technol.* **2019**, *9*, 2163-2172.

[11] Bozo, C.; Guilhaume, N.; Garbowski, E.; Primet, M. Combustion of Methane on CeO_2-ZrO_2 Based Catalysts. *Catal. Today* **2000**, *59*, 33-45.

[12] Pengpanich, S.; Meeyoo, V.; Rirksomboon, T.; Bunyakiat, K. Catalytic Oxidation of Methane Over CeO_2-ZrO_2 Mixed Oxide Solid Solution Catalysts Prepared Via Urea Hydrolysis. *Appl. Catal. A* **2002**, *234*, 221-233.

[13] Larrondo, S.; Vidal, M.; Irigoyen, B.; Craievich, A.; Lamas, D.; Fábregas, I.; Lascalea, G.; Walsoe de Reca, N.; Amadeo, N. Preparation and Characterization of Ce/Zr Mixed Oxides and Their Use as Catalysts for the Direct Oxidation of Dry CH_4. *Catalysis Today* **2005**, *107-108*, 53-59.

[14] Hao, Y.; Yang, C.K.; Haile, S. Ceria−Zirconia Solid Solutions ($Ce_{1-x}Zr_xO_{2-\delta}$, $x \leq 0.2$) for Solar Thermochemical Water Splitting: A Thermodynamic Study. *Chem. Mat.* **2014**, *26*, 6073-6082.

[15] Yashima, M.; Arashi, H.; Kakihana, M.; Yoshimura, M. Raman Scattering Study of Cubic-Tetragonal Phase Transition in $Zr_{1-x}Ce_xO_2$ Solid Solution. *J. Am. Ceram. Soc.* **1994**, *77*, 1067-1071.

[16] Yang, Z.; Woo, T.; Hermansson, K. Effects of Zr Doping on Stoichiometric and Reduced Ceria: A First-Principles Study. *J. of Chem. Phys*. **2006**, *124*, 224704.

[17] Yang, Z.; Wei, Y.; Fu, Z.; Lu, Z.; Hermansson, K. Facilitated Vacancy Formation at Zr-Doped Ceria (111) Surfaces. *Surf. Sci.* **2008**, *602,* 1199–1206.

[18] Hu, Z.; Metiu, H. Effect of Dopants on the Energy of Oxygen-Vacancy Formation at the Surface of Ceria: Local or Global? *J. Phys. Chem. C* **2011**, *115*, 17898-17909.

[19] Chen, H. T.; Chang, J. G. Oxygen Vacancy Formation and Migration in $Ce_{1-x}Zr_xO_2$ Catalyst: A DFT+U Calculation. *J. Chem. Phys.* **2010**, *132*, 214702.

[20] Tang,Y.; Zhang, H.; Cui, L.; Ouyang, C.; Shi, S.; Tang, W.; Li, H.; Lee, J. S.; Chen, L. First-Principles Investigation on Redox Properties of M-Doped CeO_2 (M=Mn, Pr, Sn, Zr). *Phys. Rev. B* **2010**, *82*, 125104.

[21] Wang, H. F.; Guo, Y. L.; Lu, H. S.; Hu, P. Maximizing the Localized Relaxation: The Origin of the Outstanding Oxygen Storage Capacity of k-$Ce_2Zr_2O_8$. *Angew. Chem. Int. Ed.* **2009**, *48*, 8289-8292.

[22] Wang, H. F.; Li, H. Y.; Gong, X. Q.; Guo, Y. L.; Lu, H. Z.; Hu, P. Oxygen Vacancy Formation in CeO_2 and $Ce_{1-x}Zr_xO_2$Solid Solutions: Electron Localization, Electrostatic Potential and Structural Relaxation. *Phys. Chem. Chem. Phys.* **2012**, *14*, 16521-16535.

[23] Wang, H. F.; Gong, X. Q.; Guo, Y. L.; Guo, Y.; Lu, G. Z.; Hu, P. A Model to Understand the Oxygen Vacancy Formation in Zr-Doped CeO_2: Electrostatic Interaction and Structural Relaxation. *J. Phys. Chem. C* **2009**, *113*, 10229-10232.

[24] Zhang, Ce; Wen, X. D.; Teng, B. T.; Zhao, Y.; Fan, M. Catalytic Effects of Zr doping ion on ceria-based catalyst. *Fuel Process. Technol.* **2015**, *131*, 1-6.

[25] Mayernick A. D.; Janik M. J. Methane Activation and Oxygen Vacancy Formation Over CeO_2 and Zr, Pd Substituted CeO_2 Surfaces. *J. Phys. Chem. C* **2008**, *112*, 14955-14964.

[26] Krcha M. D.; Mayernick A. D.; Janik M. J. Periodic Trends of Oxygen Vacancy Formation and C–H Bond Activation Over Transition Metal-Doped CeO_2 (111) Surfaces. *J. of Catalysis* **2012**, *293*, 103-115.

[27] Dudarev, S.; Botton, G.; Savrasov, S.; Humphreys, C.; Sutton, A. Electron-Energy-Loss Spectra and the Structural Stability of Nickel Oxide: An LSDA+U Study. *Phys. Rev. B* **1998**, *57*, 1505−1509.

[28] Bishop, S. R.; Marrocchelli, D.; Fang, W.; Amezawa, K.; Yashirod, K.; Watson, G. W. Reducing the Chemical Expansion Coefficient in Ceria by Addition of Zirconia. *Energy & Environ. Sci.* **2013**, 6, 1142-1146.

[29] Weck, P. F.; Juan, P.-A.; Dingreville, R.; Kim, E. Density Functional Analysis of Fluorite-Structured (Ce,Zr)O/CeO Interfaces. *J. Phys. Chem. C* **2017**, *121*, 14678-14687.

[30] Esch, F.; Fabris, S.; Zhou, L.; Montini, T.; Africh, C.; Fornasiero, P.; Comelli, G.; Rosei R. Electron Localization Determines Defect Formation on Ceria Substrates. *Science* **2005**, *309*, 752–755.

[31] Fabris, S.; Vicario, G.; Balducci, G.; de Gironcoli, S.; Baroni, S. Electronic and Atomistic Structures of Clean and Reduced Ceria Surfaces. *J. Phys. Chem. B* **2005**, *109*, 22860-22867.

[32] Ganduglia-Pirovano, M. V.; Murgida, G.; Ferrari, V.; Llois, A. M. Comment on "Oxygen Vacancy Ordering and Electron Localization in CeO_2: Hybrid Functional Study". *J. Phys. Chem. C* **2017**, *121*, 21080−21083.

[33] Murgida, G.; Ferrari, V.; Ganduglia-Pirovano, M. V.; Llois, A. M. Ordering of Oxygen Vacancies and Excess Charge Localization in Bulk Ceria: A DFT+U study. *Phys. Rev. B* **2014**, *90*, 115120.

[34] Allen, J. P.; Watson, G. W. Occupation Matrix Control of d- and f-electron Localizations using DFT+U. *Phys. Chem. Chem. Phys.* **2014**, *225*, 21016−21031.

[35] Kullgren, J.; Hermansson, K.; Castleton, C. Many Competing Ceria (110) Oxygen Vacancy Structures: From Small to Large Supercells. *J. Chem. Phys.* **2012**, *137*, 044705.

[36] Ganduglia-Pirovano, M. V.; Da Silva, J. L. F.; Sauer, J. Density-Functional Calculations of the Structure of Near-Surface Oxygen Vacancies and Electron Localization on CeO_2(111). *Phys. Rev. Lett.* **2009**, *102*, 026101.

[37] Jerratsch, J.-F.; Shao, X.; Nilius, N.; Freund, H.-J.; Popa, C.; Ganduglia-Pirovano, M. V.; Burow, A.; M.; Sauer, J. Electron Localization in Defective Ceria Films: A Study with Scanning-Tunneling Microscopy and Density-Functional Theory. *Phys. Rev. Lett.* **2011**, *106*, 246801.

[38] Murgida, G.; Ganduglia-Pirovano, M. V. Evidence for Subsurface Ordering of Oxygen Vacancies on the Reduced CeO_2 (111) Surface Using Density-Functional and Statistical Calculations. *Phys. Rev. Lett.* **2013,** *110*, 246101.

[39] Li, H.-Y.; Wang, H.-F.; Gong, X.-Q.; Guo, Y.-L.; Guo, Y.; Lu, G.; Hu, P. Multiple Configurations of the Two Excess 4f Electron on Defective CeO_2 (111): Origin and Implications. *Phys. Rev. B* **2009**, *79*, 193401.

[40] Torbrugge, S.; Reichling, M.; Ishiyama, A.; Morita, S.; Custance, O. Evidence of Subsurface Oxygen Vacancy Ordering on Reduced CeO_2 (111). *Phys. Rev. Lett.* **2007**, *99*, 056101.

[41] Han, Z. -K.; Yang, Y. -Z.; Zhu, B.; Ganduglia-Pirovano, M. V.; Gao, Y. Unraveling the Oxygen Vacancy Structures at the Reduced CeO_2 (111) Surface. *Phys. Rev. Materials* **2018**, 2, 035802.

[42] Zhang, D.; Han, Z. -K.; Murgida, G.;Ganduglia-Pirovano, M. V.; Gao, Y. Oxygen-Vacancy Dynamics and Entanglement with Polaron Hopping at the Reduced CeO_2 (111) Surface. *Phys. Rev. Lett.* **2019**, *122*, 096101.

[43] Payne, M.; Teter, M.; Allan, D.; Arias, T.; Joannopoulos, J. Iterative Minimization Techniques for Ab Initio Total-Energy Calculations: Molecular Dynamics and Conjugate Gradients. *Rev. Mod. Phys.* **1992**, *64*, 1045−1097.

[44] Kresse, G.; Hafner, J. Ab Initio Molecular Dynamics for Liquid Metals. *Phys. Rev. B* **1993**, *47*, 558−561.

[45] Kresse, G.; Furthmüller, J. Efficient Iterative Schemes for Ab Initio Total-Energy Calculations Using a Plane-Wave Basis Set. *Phys. Rev. B* **1996**, *54*, 11169−11186.

[46] Perdew, J. P.; Burke, K.; Ernzerhof, M. Generalized Gradient Approximation Made Simple. *Phys. Rev. Lett.* **1996**, *77*, 3865−3868.

[47] Cococcioni, M.; de Gironcoli, S. Linear Response Approach to the Calculation of the Effective Interaction Parameters in the LDA + U Method. *Phys. Rev. B* **2005**, *71*, 035105.

[48] Fabris, S.; de Gironcoli, S.; Baroni, S.; Vicario, G.; Balducci, G. Taming Multiple Valency with Density Functionals: A Case Study of Defective Ceria. *Phys. Rev. B* **2005**, *71*, 041102.

[49] Monkhorst, H. J.; Pack, J. D. Special Points for Brillouin-Zone Integrations. *Phys. Rev. B* **1976**, *13*, 5188−5192.

[50] Smith, D.; Newkirk H.; The Crystal Structure of Baddeleyite (Monoclinic ZrO_2) and Its Relation to the Polymorphism of ZrO_2. *Acta Cryst.* **1965**, *18*, 983-991.

[51] Teufer, G. The Crystal Structure of Tetragonal ZrO_2. *Acta Cryst.* **1962**, *15*, 1187.

[52] Aldebert, P.; Traverse, J. P. Structure and Ionic Mobility of Zirconia at high Temperature. *J. Am. Ceram. Soc.* **1985**, *68*, 34-40.

[53] Sorensen, O. Thermodynamics Studies of the phase Relationships of Nonstoichiometric Cerium Oxides at High Temperatures. *J. Solid State Chem*. **1976**, *18*, 217-233.

[54] Kümmerle, E.; Heger, G. The Structures of C-$Ce_2O_{3+\delta}$, Ce_7O_{12} and $Ce_{11}O_{20}$. *J. Solid State Chem.* **1999**, *147*, 485-500.

[55] Bärnighausen H.; Schiller, G. The Crystal Structure of A-CeO_2. *J. Less Common Metals* **1985**, *110*, 385-390.

This is the version submitted to jpc c on october 7, 2019

TOC figure

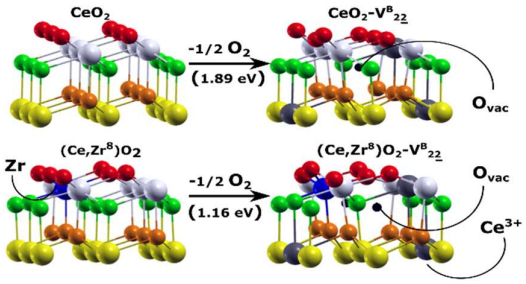

This is the version submitted to jpc c on october 7, 2019

Supporting Information

Table S1. Calculated change in the surface energy, $\Delta\Gamma$(J/m^2), as function of Zr concentration, ϑ (ML), for different dopant configurations (cf. Figure 1). $\Delta\Gamma_{unrelaxed}-\Delta\Gamma_{relax}$ is the amount by which the surface energy is lowered due to lattice relaxations in the presence of the Zr dopants. In the "scheme" column, the solid circle indicates the Zr atoms in each trilayer.

Cell	Zr atom location	ϑ	Scheme	$\Delta\Gamma_{unrelaxed}$	$\Delta\Gamma_{relax}$	$\Delta\Gamma_{unrelaxed}-\Delta\Gamma_{relax}$
1×1	Zr_{TL1}	1	● ○ ○ ○ ○	1.552[a]	1.003[a]	0.549
	Zr_{TL2}		○ ● ○ ○ ○	1.017[a]	0.330[a]	0.687
	Zr_{TL3}		○ ○ ● ○ ○	1.022	0.367	0.655
	Zr_{TL4}		○ ○ ○ ● ○	1.036	0.343	0.693
2×2	Zr^{8}	1/4	● ○ ○	0.425	0.172	0.253
	Zr^{13}		○ ● ○	0.247	0.118	0.129
	Zr^{19}		○ ○ ●	0.283	0.135	0.148
	Zr^{13}-Zr^{7}	1/2	● ● ○	0.637	0.252	0.385

This is the version submitted to jpc c on october 7, 2019

	Zr^{13}-Zr^{16}			0.473	0.218	0.255
	Z^{13}-Zr^{17}			0.507	0.260	0.247
	Zr^{13}-Zr^{16}-Zr^{8}	3/4		0.875	0.335	0.540
	Zr^{13}-Zr^{15}-Zr^{16}			0.696	0.289	0.407
	Zr^{13}-Zr^{16}-Zr^{17}			0.731	0.337	0.394
	Zr^{8}-Zr^{13}-Zr^{17}			0.719	0.356	0.363
2×2	Zr^{13}-Zr^{15}-Zr^{16}-Zr^{17}	1		0.954	0.368	0.586
	Zr^{13}-Zr^{17}-Zr^{18}-Zr^{20}			1.033	0.368	0.665
	Zr^{13}-Zr^{16}-Zr^{17}-Zr^{20}			0.991	0.308	0.683
	Zr^{7}-Zr^{8}-Zr^{13}-Zr^{16}			1.279	0.500	0.779
	Zr^{7}-Zr^{8}-Zr^{17}-Zr^{18}			1.349	0.639	0.710
	Zr^{6}-Zr^{13}-Zr^{16}-Zr^{17}			1.134	0.423	0.711
	Zr^{5}-Zr^{6}-Zr^{7}-Zr^{8}			1.644[a]	1.001[a]	0.643
	Zr^{13}-Zr^{14}-Zr^{15}-Zr^{16}			0.917[a]	0.313[a]	0.604

3×3	Zr^{1}	1/9	● ○ ○	0.173	0.080	0.093
	Zr^{10}		○ ● ○	0.119	0.053	0.066
	Zr^{1}-Zr^{2}	2/9	●● ○ ○	0.346	0.166	0.180
	Zr^{1}-Zr^{5}		●● ○ ○	0.346	0.155	0.191
	Zr^{10}-Zr^{11}		○ ● ● ○	0.237	0.105	0.132
	Zr^{10}-Zr^{15}		○ ● ● ○	0.237	0.102	0.135
	Zr^{1}- Zr^{2}... Zr^{8}- Zr^{9}	1	●.....● ○ ○	1.563[a]	1.011[a]	0.552
	Zr^{10}- Zr^{11}... Zr^{17}- Zr^{18}		○ ●.....● ○	1.060[a]	0.308[a]	0.752

[a]The energy difference between the $\Delta\Gamma$ values obtained from calculations with 1, 4, or 9 Zr dopants in either TL1 or TL2 with (1×1), (2×2), and (3×3), respectively, should be negligible because they all correspond to 1 ML. Small differences are likely to originate to differences in the number of Ce–O–Ce trilayers and the thickness of the vacuum layer in the slabs, namely, 6 TL and 17 Å, 5 TL and 10 Å, and 4 TL and 14.5 Å, respectively.

Table S2. Average bond lengths within the first, second and third coordination shell (CS) of the Ce (Zr) atoms in TL1, TL2 and TL3 in CeO_2[$(Ce,Zr)O_2$] (111). The difference (Δ) between the average Ce–O and Zr–O bond lengths with O either in the first or third coordination shell of the cations, as well as that between the average Ce–Ce and Zr–Ce bond lengths, are also included.

	Bond length (pm) in CeO_2				Bond length (pm) in $(Ce,Zr)O_2$			Δ (pm)		
	Ce–O	Ce–Ce	Ce–O		Zr–O	Zr–Ce	Zr–O			
CS	1	2	3	CS	1	2	3	1	2	3
TL1	236.9	387	452.7	TL1 (Zr^{8})	227.4	384.7	449.8	9.5	2.3	2.9
TL2	236.9	386.7	453.6	TL2 (Zr^{13})	228	384.8	452.1	8.9	1.9	1.5
TL3	236.8	387.3	454.5	TL3 (Zr^{19})	228.5	385.9	453.7	8.3	1.4	0.8

This is the version submitted to jpc c on october 7, 2019

Table S3. Near-surface oxygen vacancy formation energy at the (Ce,Zr)O_2 (111) surface, E_f (eV), for several configurations with respect to the locations of the Zr dopant, the vacancy, and the associated Ce^{3+} ions. The structures are labeled $Zr^{8/13}$- $V^{A/B}{}_{nm}$, where $Zr^{8/13}$ denote the dopant location ($Zr^{TL1/TL2}$, cf. Figure 1), $V^{A/B}$ the vacancy location ($V^{TL1/TL2}$), and the sub-indices *n* and *m* denote the neighboring cationic coordination shells in which the two Ce^{3+} are located. Selected distances are given in Å. The shortest distance is included in those cases with multiple options.

Configuration		E_f **(eV)**	**Zr–$V^{A/B}$**	**$V^{A/B}$–Ce^{3+}**		**Ce^{3+}–Zr**		**Ce^{3+}–Ce^{3+}**
Zr–$V^{A/B}{}_{nm}$	$Zr^{\#}$–$V^{\#}{}_{\#,\#}$							
Zr^8–$V^A{}_{2\underline{3}}$	Zr^8–$V^4{}_{7,\underline{15}}$	1.62	2.40	4.38	5.80	3.91	3.67	5.66
Zr^8–$V^A{}_{11}$	Zr^8–$V^4{}_{5,6}$	1.87	2.44	2.55	2.55	3.57	3.57	3.70
Zr^8–$V^A{}_{2\underline{2}}$	Zr^8–$V^1{}_{5,\underline{14}}$	1.32	2.43	4.40	4.45	3.90	5.24	4.03
Zr^8–$V^A{}_{2\underline{2}}$	Zr^8–$V^1{}_{5,\underline{13}}$	1.35	2.48	4.42	4.25	3.90	3.69	4.05
Zr^8–$V^B{}_{2,\underline{2}}$	Zr^8–$V^{11}{}_{5,\underline{14}}$[a]	1.16	2.57	4.49	4.46	3.83	5.30	3.85
Zr^8–$V^B{}_{1\underline{2}}$	Zr^8–$V^{11}{}_{5,\underline{16}}$[b]	1.33	2.59	2.40	4.48	3.93	3.88	5.51
Zr^8–$V^B{}_{2\underline{2}}$	Zr^8–$V^{10}{}_{7,\underline{13}}$[c]	1.29	2.58	4.49	4.41	3.85	3.73	3.86
Zr^8–$V^B{}_{1\underline{1}}$	Zr^8–$V^{12}{}_{7,\underline{13}}$	1.43	2.64	2.48	2.34	3.70	3.93	4.12
Zr^8–$V^B{}_{11}$	Zr^8–$V^{12}{}_{5,7}$	1.75	2.62	2.50	2.50	3.69	3.69	3.77
Zr^8–$V^B{}_{2\underline{2}}$	Zr^8–$V^{12}{}_{6,\underline{16}}$	1.19	2.64	4.45	4.40	3.86	3.75	3.85
Zr^{13}–$V^A{}_{1\underline{2}}$	Zr^{13}–$V^2{}_{8,\underline{14}}$	2.43	5.83	2.39	4.43	3.83	3.88	5.47
Zr^{13}–$V^A{}_{11}$	Zr^{13}–$V^3{}_{6,7}$	2.18	4.45	2.46	2.48	5.45	3.84	3.68
Zr^{13}–$V^B{}_{1\underline{2}}$	Zr^{13}–$V^{12}{}_{8,\underline{15}}$	1.63	2.37	2.52	4.45	4.14	3.88	3.94
Zr^{13}–$V^B{}_{1\underline{2}}$	Zr^{13}–$V^9{}_{\underline{14},8}$	2.27	4.54	2.42	4.54	3.88	3.84	5.52
Zr^{13}–$V^B{}_{1\underline{1}}$	Zr^{13}–$V^9{}_{5,\underline{14}}$	2.59	4.50	2.51	2.41	3.95	3.83	4.08
Zr^{13}–$V^B{}_{1\underline{2}}$	Zr^{13}–$V^{12}{}_{8,\underline{16}}$[d]	1.88	2.38	2.50	4.41	4.17	3.87	4.00
Zr^{13}–$V^B{}_{2\underline{2}}$	Zr^{13}–$V^{12}{}_{6,\underline{15}}$[e]	1.26	2.37	4.51	4.41	5.57	3.87	3.86
Zr^{13}–$V^B{}_{11}$	Zr^{13}–$V^{12}{}_{5,7}$	1.76	2.38	2.53	2.53	4.12	4.12	3.77

This is the version submitted to jpc c on october 7, 2019

Zr^{13}–$V^{TL2}{}_{11}$	Zr^{13}–$V^{TL2}{}_{7,14}$[f]	1.92	2.47	2.73	2.43	4.27	3.71	4.18
Zr^{13}–$V^{TL2}{}_{11}$	Zr^{13}–$V^{TL2}{}_{15,17}$[g]	2.5	2.47	2.48	2.48	3.07	4.11	3.98
Zr^{19}–$V^{A}{}_{11}$	Zr^{19}–$V^{1}{}_{7,8}$	2.60	7.08	2.46	2.46	6.78	6.78	3.7
Zr^{19}–$V^{A}{}_{12}$	Zr^{19}–$V^{1}{}_{7,5}$	2.28	7.07	2.47	4.50	6.79	7.86	3.88
Zr^{19}–$V^{A}{}_{22}$	Zr^{19}–$V^{1}{}_{5,14}$	1.88	7.09	4.51	4.49	7.88	3.87	4.01
Zr^{19}–$V^{B}{}_{11}$	Zr^{19}–$V^{11}{}_{6,7}$	2.45	7.16	2.56	2.56	6.99	6.99	3.74
Zr^{19}–$V^{B}{}_{22}$	Zr^{19}–$V^{11}{}_{5,14}$	2.37	7.16	4.55	4.50	7.86	3.98	3.88
CeO_2–$V^{A}{}_{11}$	CeO_2–$V^{1}{}_{6,8}$	2.52	---	2.48	2.54	---		3.65
CeO_2–$V^{A}{}_{22}$	CeO_2–$V^{3}{}_{8,16}$	2.24	---	4.51	4.48	---		4.01
CeO_2–$V^{B}{}_{11}$	CeO_2–$V^{11}{}_{6,7}$	2.39	---	2.52	2.52	---		3.75
CeO_2–$V^{B}{}_{22}$	CeO_2–$V^{12}{}_{6,15}$	1.89	---	4.55	4.53	---		3.85

[a]Initialconfiguration (IC): Zr^{8}–$V^{4}{}_{5,14}$

[b] IC: Zr^{8}–$V^{4}{}_{16,5}$

[c] IC: Zr^{8}–$V^{2}{}_{7,13}$

[d] IC: Zr^{13}–$V^{3}{}_{8,16}$

[e] IC: Zr^{13}–$V^{3}{}_{6,15}$

[f,g]The oxygen vacancy is located in TL2 in the third[(f)] and fourth[(g)] oxygen layer, respectively.

Table S4. Formation energy of surface oxygen vacancies at the CeO_2 and $(Ce,Zr)O_2$ (111) surfaces, E_f (eV/atom) (cf. Table S3), Ce^{3+}–O corresponds to the average Ce^{3+}–O bond lengths (in Å) in the relaxed structures.

System	Unrelax	Relaxed					
	E_f	E_f V^A_{11}	Ce^{3+}– O V^A_{11}		E_f $V^A_{2\underline{2}}$	Ce^{3+}– O $V^A_{2\underline{2}}$	
Clean	3.81	2.52	2.39	2.28	2.24	2.50	2.51
Zr^8	3.17	1.87	2.42	242	1.32	2.57	2.52
Zr^{13}	3.42	2.18	2.42	2.41	–	–	–
Zr^{19}	3.88	2.60	2.44	2.44	1.88	2.54	2.51

Table S5. Formation energy of subsurface oxygen vacancies at the CeO_2 and $(Ce,Zr)O_2$ (111) surfaces, E_f (eV/atom) (cf. Table S3), Ce^{3+}–O corresponds to the average Ce^{3+}–O bond lengths (in Å) in the relaxed structures.

System	Unrelax	Relaxed					
	E_f	E_f V^B_{11}	Ce^{3+}– O V^B_{11}		E_f $V^B_{2\underline{2}}$	Ce^{3+}– O $V^B_{2\underline{2}}$	
Clean	3.96	2.39	2.44	2.44	1.89	2.52	2.49
Zr^8	3.46	1.75	2.44	2.43	1.16	2.54	2.51
Zr^{13}	3.76	1.76	2.44	2.44	1.26	2.52	2.51
Zr^{19}	3.95	2.45	2.47	2.44	2.37	2.52	2.50

This is the version submitted to jpc c on october 7, 2019